SCIENTIFIC COMMUNICATIONS

AN UNUSUAL EARLY EOCENE, SYNCOLLISIONAL CARBONATITE COMPLEX AND RELATED RARE EARTH ELEMENT DEPOSIT IN THE INDIA-ASIA COLLISION ZONE, NORTHWESTERN VIETNAM

Xiao-Chun Li,[1,2,†] Mei-Fu Zhou,[3] Shi-Hu Li,[4] Xiao-Ran Zhang,[4] Hong-Rui Fan,[1,2] David I. Groves,[5] and Ngo Xuan Dac[6]

[1]*Key Laboratory of Mineral Resources, Institute of Geology and Geophysics, Chinese Academy of Sciences, Beijing 100029, China*

[2]*College of Earth and Planetary Sciences, University of Chinese Academy of Sciences, Beijing 100049, China*

[3]*School of Earth Resources, China University of Geosciences, Wuhan 430074, China*

[4]*State Key Laboratory of Lithospheric Evolution, Institute of Geology and Geophysics,
Chinese Academy of Sciences, Beijing 100029, China*

[5]*Centre for Exploration Targeting, University of Western Australia, Nedlands, Western Australia 6009, Australia*

[6]*Department of Mineral Resource Prospecting and Exploration, Hanoi University of Mining and Geology, Hanoi 100000, Vietnam*

Abstract

Carbonatite-related rare earth element (REE) deposits, the most significant source of REEs globally, are normally generated in extensional settings, such as intracontinental rifts, mantle plume-related environments, or postcollisional orogens. Syncollisional orogens represent overall compressional regimes, so carbonatites and related REE deposits are rarely identified in such a setting. However, this study reports an anomalous syncollisional carbonatite-related REE deposit, Dong Pao, in the India-Asia collision zone in northwestern Vietnam. The Dong Pao deposit is dated at ca. 52–51 Ma through zircon and bastnäsite Th-U-Pb chronometers. The ore-hosting carbonatites were emplaced as stocks with associated syenite. The carbonatite-syenite complex is significantly enriched in light REEs, Ba, and Sr and depleted in high-field strength elements, and has high $(^{87}Sr/^{86}Sr)_i$ ratios (>0.707) and low $\varepsilon_{Nd_{(t)}}$ values (–6.5 to –5.6). These geochemical signatures imply that the carbonatite-syenite complex was derived from partial melting of subcontinental lithospheric mantle previously metasomatized and fertilized by REE- and CO_2-bearing fluids. Timing of the REE-rich carbonatite-syenite complex indicates that it was related to a far-field stress within the early Eocene main-collision stage at 52–51 Ma rather than the late-collision stage at 42–35 Ma as previously thought. Collisional tectonism involving block rotation and fault activation are interpreted to have induced disturbance of the lithosphere mantle and created localized, transtensional/extensional environments oblique to the trend of the orogen that facilitated emplacement of the REE-rich carbonatitic magmas. Dong Pao appears to be the first identified, high-tonnage REE deposit that formed in the syncollisional geodynamic setting. Such a finding highlights that tectonic disturbance of an REE-rich lithosphere mantle distal to collision sutures has the potential to generate REE deposits, even during prominent convergence and collision of continents. As such, it defines additional search spaces for exploration of other REE orebodies of this style in complex collisional orogens.

Introduction

The rare earth elements (REEs) have become increasingly important in high-tech industries and are categorized as critical and strategic metals in industrialized countries. The rapid increase in global demand for REEs has promoted extensive exploration for, and exploitation of, new REE deposits. Mineral systems normally form clusters that develop in specific geodynamic settings, providing a first-order guide to identification of exploration search spaces (Groves and Bierlein, 2007; Bierlein et al., 2009).

Most of the world's REE deposits are associated with mantle-derived carbonatite-(alkaline) complexes (Chakhmouradian and Wall, 2012). Carbonatitic melts are highly reactive and are important agents for metasomatism of the mantle. Thus, a majority of carbonatitic melt is consumed by reaction with mantle rocks and undergoes chemical death (Dalton and Wood, 1993; Bell et al., 1998). An extensional tectonic environment is favored to facilitate rapid transport

and emplacement of the melt so that it can be preserved in the crust. Therefore, carbonatites and related REE deposits are commonly generated by anorogenic processes, which are associated with intraplate rifting or uprise of plumes (Pirajno, 2015; Goodenough et al., 2016; Simandl and Paradis, 2018). Typical examples include the world-class Bayan Obo REE deposit in China (Yang, K.F., et al., 2019), the Palabora REE-rich phoscorite-carbonatite complex in South Africa (Giebel et al., 2019), the Amba Dongar REE-rich carbonatite complex in India (Chandra et al., 2019), and the carbonatite-alkaline complexes in the Kola Peninsula, Russia (Zaitsev et al., 2014). Postcollisional settings in an orogen may include tectonic events such as lithosphere delamination, large-scale faulting, and/or rift generation (Liegeois, 1998; Hou and Cook, 2009). These events include continuous or episodic extensional regimes, so relatively rare carbonatites and REE deposits can be generated in a postcollisional setting, as for the Eden Lake carbonatite in the Trans-Hudson orogen, Canada (Chakhmouradian et al., 2008), Naantali carbonatite in southwestern Finland (Woodard and Hetherington, 2014),

1

the REE-rich carbonatite-syenite complex in the South Qin-ling orogen, China (Zhang et al., 2019), and the REE-rich carbonatite in the Hongcheon area, Korea (Kim et al., 2016). In contrast, syncollisional orogen is generally operated in a compressional regime, which is not favorable for the ascent of magmas and fluids (Marignac and Cuney, 1999). Indeed, carbonatites and REE deposits do not appear to have been identified previously in a syncollisional setting.

The Tibetan orogen, which was generated through the collision between the India and Asia plates, is the best-preserved global example of a collisional orogen (Yin and Harrison, 2000; Fig. 1). In this relatively young orogen, all stages of India-Asia convergence can be recorded, and detailed relationships to ore formation, commonly reflect-ing tectonic changes measured on million-year timescales, can be accurately documented. Several large Cenozoic (ca. 28–12 Ma) carbonatite-related REE deposits have been identified on the eastern Tibetan Plateau in southwestern China (Fig. 2). These REE deposits were associated with large-scale strike-slip faulting and resultant extensional fracture zones in the late/postcollisional period (Hou et al., 2009; Xie et al., 2015).

Large carbonatite-related REE deposits have also been identified to the southeast of the Tibetan Plateau in north-western Vietnam, with Dong Pao and Nam Xe as repre-sentative examples (Tran et al., 2016; Fig. 2). However, the mineralization age and tectonic setting of these deposits remain poorly constrained. In order to better understand the relationship between REE mineralization and collision-related events, Th-U-Pb dating was conducted on ore-related zircon and bastnäsite from the Dong Pao deposit. The dating yielded high-precision ages of 52.4–51.4 Ma for this deposit, apparently older than the Cenozoic REE deposits in south-western China. Many studies have suggested that the India-Asia collision initially occurred in the late Paleocene to early Eocene (55 ± 5 Ma, Najman et al., 2010; Donaldson et al., 2013; DeCelles et al., 2014; Hu et al., 2015; Ding et al., 2017; Bian et al., 2021; Fig. 3). Continuous India-Asia convergence led to intensive crustal shortening and thickening, large-scale thrusting, and high-grade metamorphism in the early Eocene (Yin and Harrison, 2000; Aikman et al., 2008; Ding et al., 2016). Thus, the new age data for the Dong Pao deposit indi-cate that it was formed during the period of overall conver-gence and collision between India and Asia (Fig. 3). To our
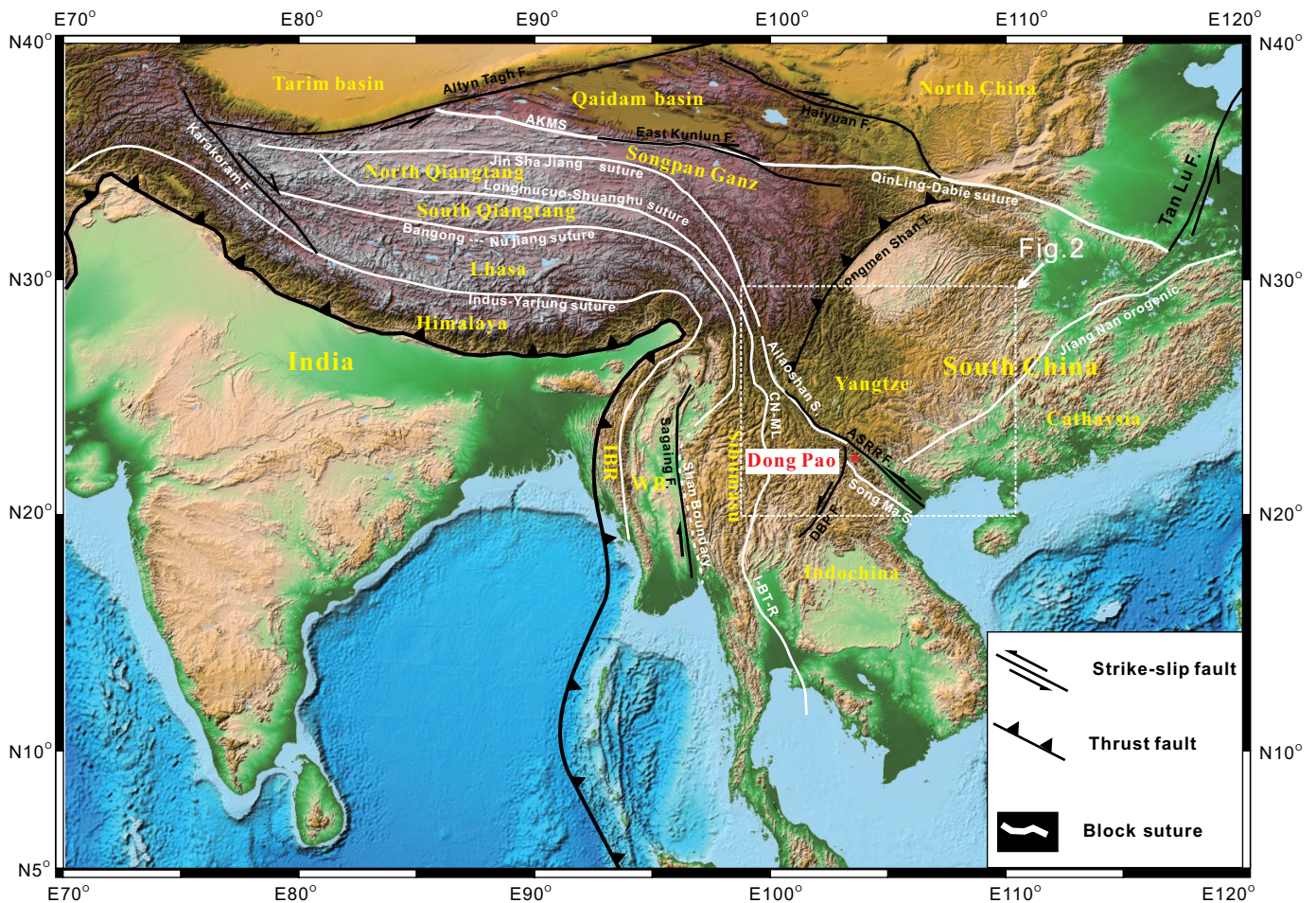

Fig. 1. (a) Simplified map showing main tectonic units of the Tibetan Plateau and adjacent regions. The white and black lines represent major sutures and faults, respectively. Abbreviations: AKMS = Anyimaqin-Kunlun-Muztagh suture, ASRR = Ailao Shan-Red River shear zone, CN-ML = Changning-Menglian suture, DBPF = Dien Bien Phu fault, IBR = Indo-Burma Ranges, I-BT-R = Inthanon-Bentong-Raub suture, WB = West Burma block.
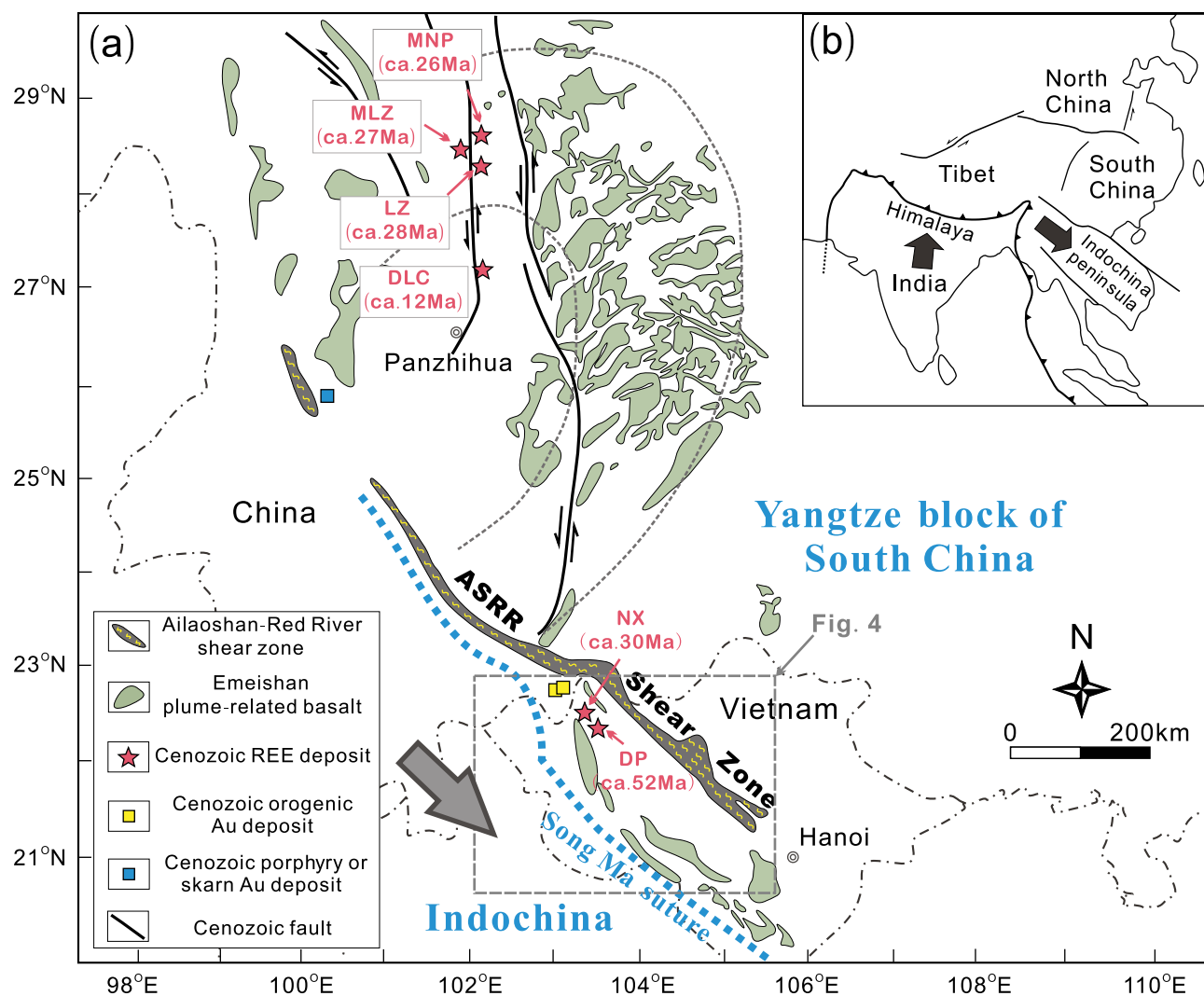
Fig. 2. (a) Simplified regional-scale geotectonic map of northwestern Vietnam and southwestern China, highlighting the distribution of Emeishan plume-related basalt, Cenozoic carbonatite-related rare earth element (REE) deposits, orogenic Au deposits, and porphyry-skarn Au deposits. Note that the distribution of Emeishan plume-related basalt clearly indicates southeastern displacement of the Indochina Peninsula relative to South China. The area covered by the district-scale geologic map in Figure 4 is marked. (b) Major Cenozoic fault systems in Asia (after Tapponnier et al., 1990), illustrating continent extrusion in response to India-Asia collision. Abbreviations: ASRR = Ailao Shan-Red River, DLC = Dalucao deposit, DP = Dong Pao deposit, LZ = Lizhuang deposit, MLZ = Muluozhai deposit, MNP = Maoniuping deposit, NX = Nam Xe deposit.

knowledge, Dong Pao is the first syncollisional REE deposit to be unequivocally identified around the India-Asia collision zone and possibly even globally.

In this paper, whole-rock geochemistry and C-O and Sr-Nd isotopes are employed to constrain the petrogenesis of the carbonatite-syenite complex hosting the Dong Pao deposit. This information, combined with published geologic data from the region, is used to discuss the geodynamic triggers that could have been responsible for the formation of this unusual REE deposit. On a broader scale, the features of all Cenozoic REE deposits around the Tibetan orogen are synthesized, and optimal factors that facilitate the formation of collision related REE deposits are outlined. Furthermore, the implications for potentially new exploration search spaces based on the newly identified Dong Pao REE deposit are discussed.

Regional Geology

Tectonic framework of the Tibetan Plateau and adjacent regions

The Tibetan Plateau and adjacent regions constitute a complex collage of continental blocks, which include South China (including the western Yangtze block and eastern Cathaysia block), Indochina, Sibumasu, and West Burma in the east, and India, Himalaya, Lhasa, South and North Qiangtang, and the Songpan-Ganzi flysch belt in the west (Fig. 1). These blocks are interpreted to have separated from Gondwana since the early Paleozoic and drifted to the north and eventually accreted to the Eurasian continent (Metcalfe, 2013). Amalgamation of these blocks was associated with the closure of the Paleo-Tethys Ocean from the Devonian to Triassic,
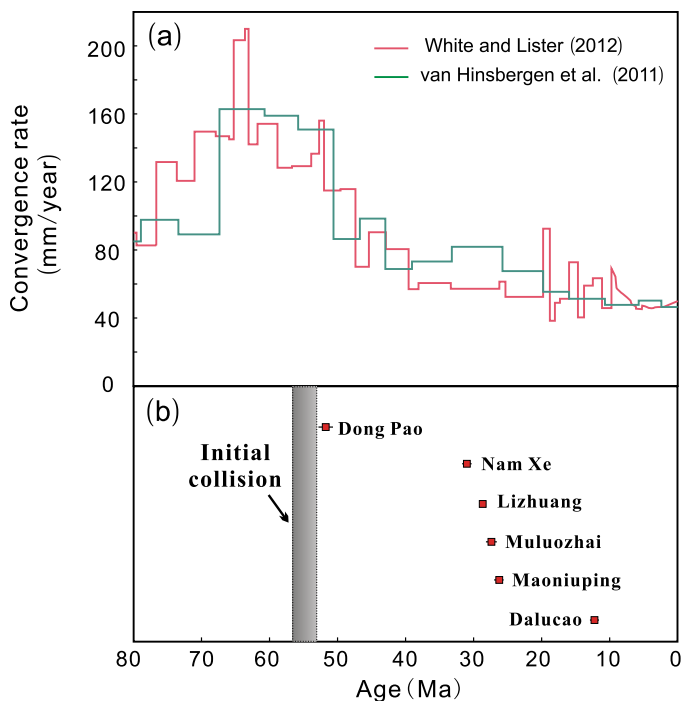
Fig. 3. (a) Temporal variation in India-Asia convergence rates (van Hinsbergen, 2011; White and Lister, 2012). (b) Summary of isotopic ages of Cenozoic carbonatite-related rare earth element deposits around the Tibetan Plateau (Thi et al., 2014; Ling et al., 2016; this study). The timing of initial India-Asia collision (according to Najman et al., 2010; Donaldson et al., 2013; Hu et al., 2015; Ding et al., 2017; Bian et al., 2021) is shown for reference.

the Meso-Tethys Ocean from the early Permian to Late Cretaceous, and the Neo-Tethys Ocean from the Late Triassic to Cenozoic (Metcalfe, 2013). The Paleo-Tethys suture marks the collisions of the Qiangtang-Indochina blocks with the South China block and Sibumasu with Indochina along the Jinshajiang belt in central Tibet and the Ailaoshan and Changning-Menglian belts in southwestern China (Wang, X., et al., 2000; Wang, Y., et al., 2018). The Meso-Tethys suture was formed by the collisions of Lhasa with Qiangtang and West Burma with Sibumasu (Liu et al., 2016; Zhu et al., 2016), is exposed along the Bangong-Nujiang suture in central Tibet, and continues southeastward to the Myitkyina suture in eastern Myanmar. The Neo-Tethys suture, which represents the collision of India and Asia, includes the Indus-Yarlung suture in southern Tibet and the Kalaymyo suture in the Indo-Burman Ranges (Aitchison et al., 2002; Liu et al., 2016).

The Tibetan Plateau and adjacent regions have experienced strong deformation in response to the India-Asia collision. The early stage of deformation (ca. 55–40 Ma) was mainly characterized by crustal shortening and thickening (Yin and Harrison, 2000; Tapponnier et al., 2001; Aikman et al., 2008; Cao et al., 2021). With ongoing continent-continent convergence, crustal shortening and thickening could not absorb all compressive stresses, and strike-slip faulting, vertical axis rotation, and block extrusion developed since the middle Eocene (ca. 40 Ma; Tapponnier et al., 1990; Leloup et al., 1995; Li et al., 2017). Since the mid-Miocene (ca. 15 Ma), a series of normal fault systems developed across the Tibetan Plateau (Burchfiel et al., 1992; Blisniuk et al., 2001) in response to

an extensional/transtensional regime that operated on the plateau. Deformation in southeastern Tibet was characterized by early crustal shortening followed by southeastward extrusion and clockwise rotation of blocks via large-scale strike-slip faults. The nearly 1,000-km-long Ailao Shan-Red River shear zone, extending from southeastern Tibet to the northern South China Sea, defines a prominent crustal discontinuity (Leloup et al., 1995). Activation of the Ailao Shan-Red River shear zone led to southeastward displacement of the Indochina Peninsula (the Indochina block and a small portion of the South China block) relative to South China by over 500 km (Tapponnier et al., 1990; Leloup et al., 1995; Fig. 2).

Geology of northwestern Vietnam

The Dong Pao deposit is located in northwestern Vietnam, where it is bounded by the Red River fault to the north and the Song Ma suture belt to the south (Fig. 4). The geology of northwestern Vietnam is characterized by two major tectono-thermal events. One is the Triassic (ca. 250 Ma) amalgamation of South China and Indochina along the Song Ma suture belt (Faure et al., 2014). The other is the activation of the Ailao Shan-Red River shear zone and southeastward extrusion of the Indochina Peninsula. Thus, northwestern Vietnam represents a southeastward-displaced portion of the Yangtze block of South China (Chung et al., 1997).

In northwestern Vietnam, a metamorphic complex, which includes the Suoi Chieng and Sin Quyen Formations, is distributed along the length of the Red River fault. The protoliths of the metamorphic complex include Paleo- to Neoproterozoic igneous and sedimentary rocks, which were metamorphosed to the amphibolite facies (Wang et al., 2016; Li et al., 2018a). The metamorphic complex is intruded by abundant Neoproterozoic (843–736 Ma) granitic plutons (Li et al., 2018b). The Neoproterozoic plutons, together with contemporaneous igneous rocks (ca. 860–730 Ma) in southwestern China, form a large-scale continental-arc belt, corresponding to oceanic subduction beneath the Yangtze block in the Neoproterozoic (Li et al., 2018b). Phanerozoic strata, dominated by Silurian-Triassic clastic-carbonate sequences, are widely distributed in northwestern Vietnam, together with late Permian plume-related rocks (ca. 260–256 Ma), including basalt, rhyolite, and alkaline granite (Tran et al., 2015; Usuki et al., 2015). Before the southeastward displacement of northwestern Vietnam, the plume-related rocks were originally located within the inner zone of the Emeishan large igneous province in the western Yangtze block (Chung et al., 1997; Usuki et al., 2015; Fig. 2).

In response to the India and Asia collision, a series of Cenozoic magmas were intruded in northwestern Vietnam to produce the Dong Pao and Nam Xe carbonatite-(syenite) complexes (Thi et al., 2014), the Pu Sam Cap and Chinh Sang high-K alkaline intrusions (ca. 40–32 Ma; Tran et al., 2014; Pham et al., 2020), and many lamprophyre dikes (ca. 40–35 Ma; Yang et al., 2013; Tran et al., 2016). Extensive Cenozoic magmatism is also documented in southwestern China, with the formation of similar rock types that include ca. 28–11 Ma carbonatite-alkaline complexes (Hou et al., 2006), ca. 40–24 Ma lamprophyres (Guo et al., 2005), and ca. 37–33 Ma potassic felsic intrusions (Lu et al., 2013). The carbonatite complexes are commonly associated with REE mineralization that formed
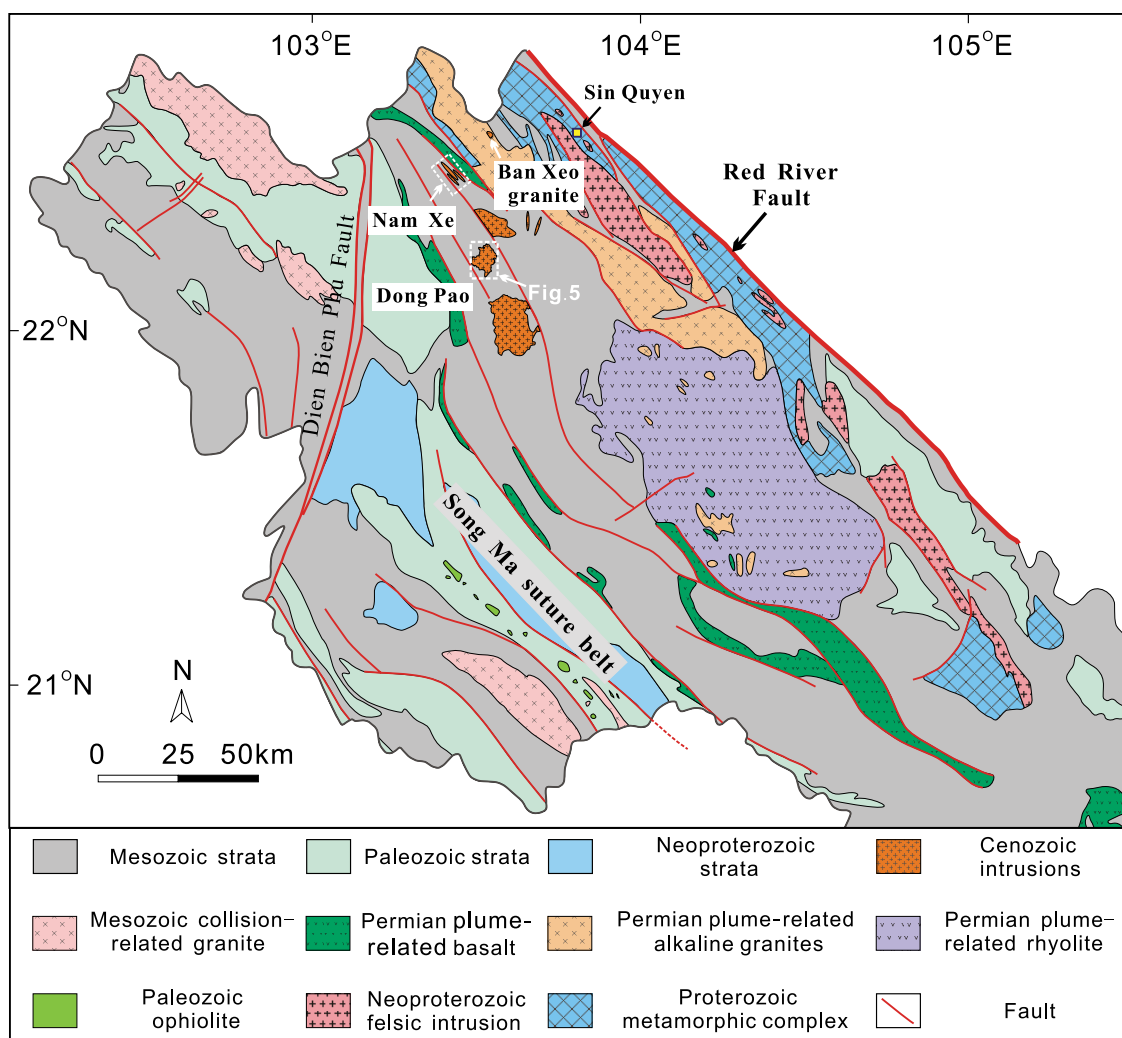
Fig. 4. District-scale geologic map of northwestern Vietnam representing the southern section of the more regional map in Figure 2 (modified from Tran, 2000). The Dong Pao, Nam Xe, and Sin Quyen deposits and the Ban Xeo A-type granite are marked by arrows. The specific ore district for Dong Pao shown in Figure 5 is outlined.

the Maoniuping, Dalucao, Lizhuang, and Muluozhai REE deposits (Hou et al., 2006; Fig. 2).

Several high-tonnage REE deposits, including the Sin Qyen, Nam Xe, and Dong Pao deposits, are distributed in northwestern Vietnam (Fig. 4). The Sin Quyen deposit occurs in the high-grade metamorphic complex adjacent to the Red River fault. It is interpreted to be an iron oxide copper-gold deposit, which has a close genetic association with Neoproterozoic (ca. 840 Ma), subduction-related magmatism (Li and Zhou, 2018). Recent precise data on REE resources for the Sin Quyen deposit are not available, although Mclean (2002) provides a measured resource of 52.8 Mt ore at 0.7% light REEs with a total resource of approximately 400,000 t of light REEs. The earlier quote by Duong et al. (2021) of a total resource of 334,000 t REEs is in close agreement. In the orebodies, the REEs are mainly hosted in allanite-(Ce), which occurs in close association with iron oxides (dominated by magnetite), Cu sulfides (dominated by chalcopyrite), and silicate gangue minerals, including amphibole and biotite. The Nam Xe and Dong Pao deposits lie in a NW-SE–trending zone, defined

by a series of NW-SE–trending faults (Fig. 4). The Nam Xe deposit has a total measured resource of 1.74 Mt rare earth oxides (REOs) (Tran et al., 2016), and Dong Pao has a total measured resource of 1.5 Mt REOs (H. Van Dung, Geological Division for Radioactive and Rare Elements, General Department of Geology and Minerals of Vietnam, pers. commun., 2021). For both deposits, the REE ores have been previously interpreted to have been generated from aqueous-carbonic fluids exsolved from Cenozoic alkaline magmas from which carbonatite-syenite complexes crystallized (Japan International Cooperation Agency [JICA] and Metal Mining Agency of Japan [MMAJ], unpub. report, 2002; Thi et al., 2014). The REEs are dominantly hosted in hydrothermal fluorocarbonates such as bastnäsite and synchysite. In addition to REEs, the ores are also enriched in Ba, Sr, U, and Th.

Deposit Geology

The Dong Pao deposit was discovered in 1959. In the 1990s, the deposit was explored by the JICA and the MMAJ. Exploration on the hypogene mineralization showed a total reserve

of 0.55 Mt REOs at an average grade of 3.6 wt % (JICA and MMAJ, unpub. report, 2002). The ore district is covered by widespread REE-rich regolith, with recent exploration of this regolith defining an additional 0.9 Mt REOs at an average grade of 4 wt % (H. Van Dung, pers. commun., 2021). In addition to REEs, a few orebodies are enriched in fluorite, with a combined fluorite resource of 9.4 Mt (Tran et al., 2016).

In this deposit, the ore-hosting carbonatite-syenite complex is approximately 5 km in length and 3 km in width (Fig. 5a). The carbonatite-syenite complex intrudes limestone, shale, and sandstone of the Triassic Dong Giao Formation. In outcrop, carbonatite occurs in the inner side of the complex and occupies a smaller area than syenite. Exploration drilling shows that the carbonatite dips steeply northwest and extends
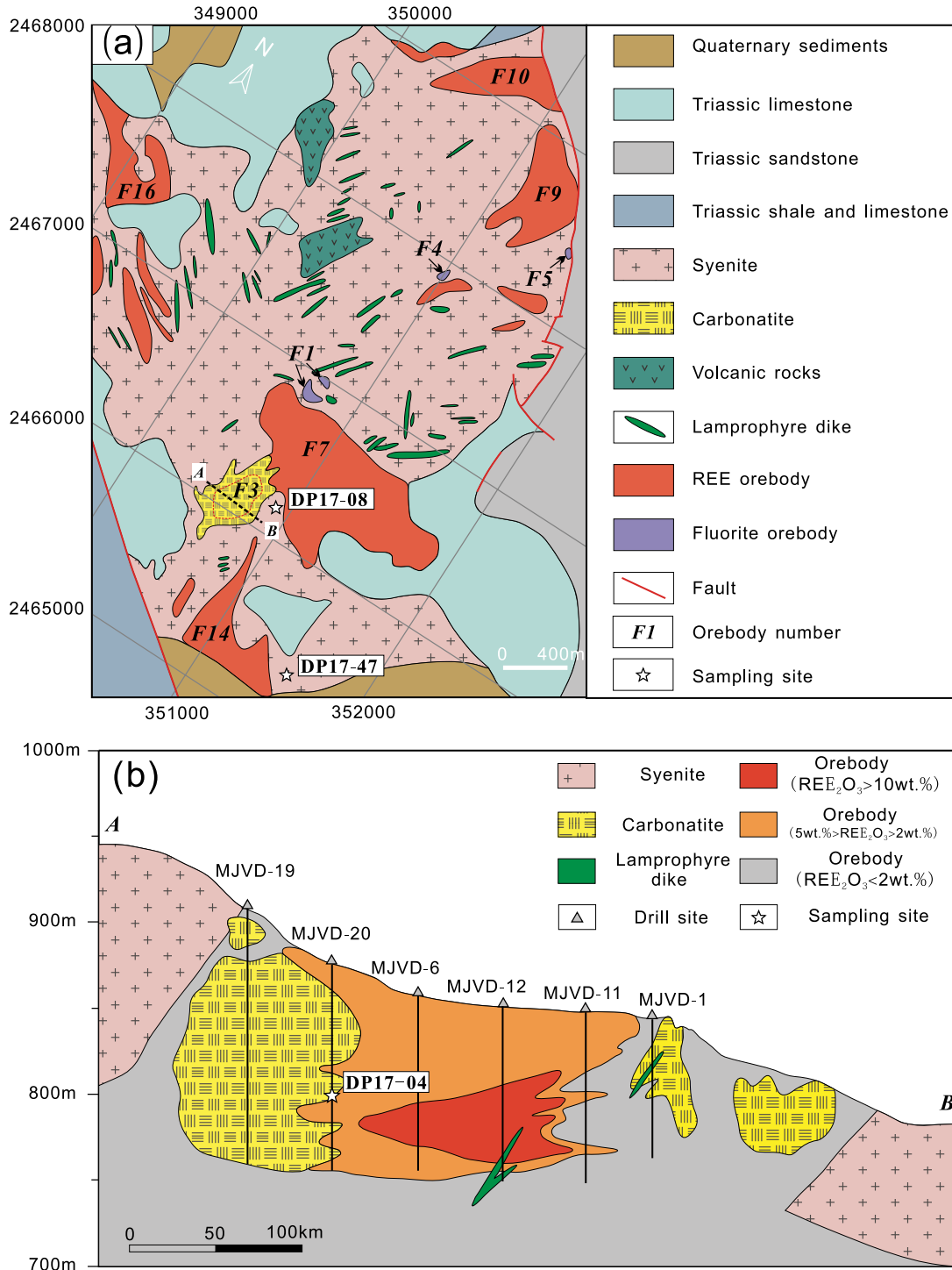

Fig. 5. (a) Simplified geologic map of the Dong Pao ore district. (b) Cross section of the F3 orebody (after JICA and MMAJ, unpub. report, 2002). REE = rare earth element.

to a depth of at least 150 m (Fig. 5b). The carbonatite-syenite complex is intruded by abundant, mostly NE-trending lamprophyre dikes. Alkaline volcanic rocks overly the syenite-carbonatite complex in parts in the Dong Pao district. The lamprophyre dikes and alkaline volcanic rocks are not mineralized and thus postdated the mineralization.

The primary carbonatite mainly consists of fine-grained (50–200 µm) calcite (>90 vol %), with minor proportions of tainiolite, apatite, pyrochlore, and barite (Fig. 6a-c). The carbonatite is commonly overprinted by later-stage hydrothermal minerals. Syenite is mainly composed of fine-grained (100–500 µm) K-feldspar (85 vol %), with subordinate quartz (<5 vol %), opaque iron oxides (<5 vol %), and biotite (<3 vol %) (Fig. 6d). Accessory minerals include zircon, apatite, and barite. Syenite samples adjacent to carbonatite commonly contain variable proportions of calcite, which is interstitial to K-feldspar grains (Fig. 6e, f).

Multiple REE orebodies can be identified at Dong Pao (Fig. 5a). The F3 orebody, which accounts for most of the proven REE reserves and contains relatively high grade hypogene REE ore, occurs in close association with the carbonatite (Fig. 5b). The other orebodies occur at the contacts between the carbonatite-syenite complex and host sedimentary rocks. The F3 orebody consists mainly of massive replacement ores (Fig. 7a), with minor vein-type varieties (Fig. 7b). The other orebodies are mainly composed of vein- and breccia-type ores (Fig. 7c, d).

Sampling and Analytical Methods

In this study, six carbonatite samples, nine syenite samples, and three ore-hosting limestone samples were collected. Carbonatite was collected from drill cores, and syenite and limestone were collected from outcrops. The main characteristics of the studied samples are listed in Appendix Table A1.
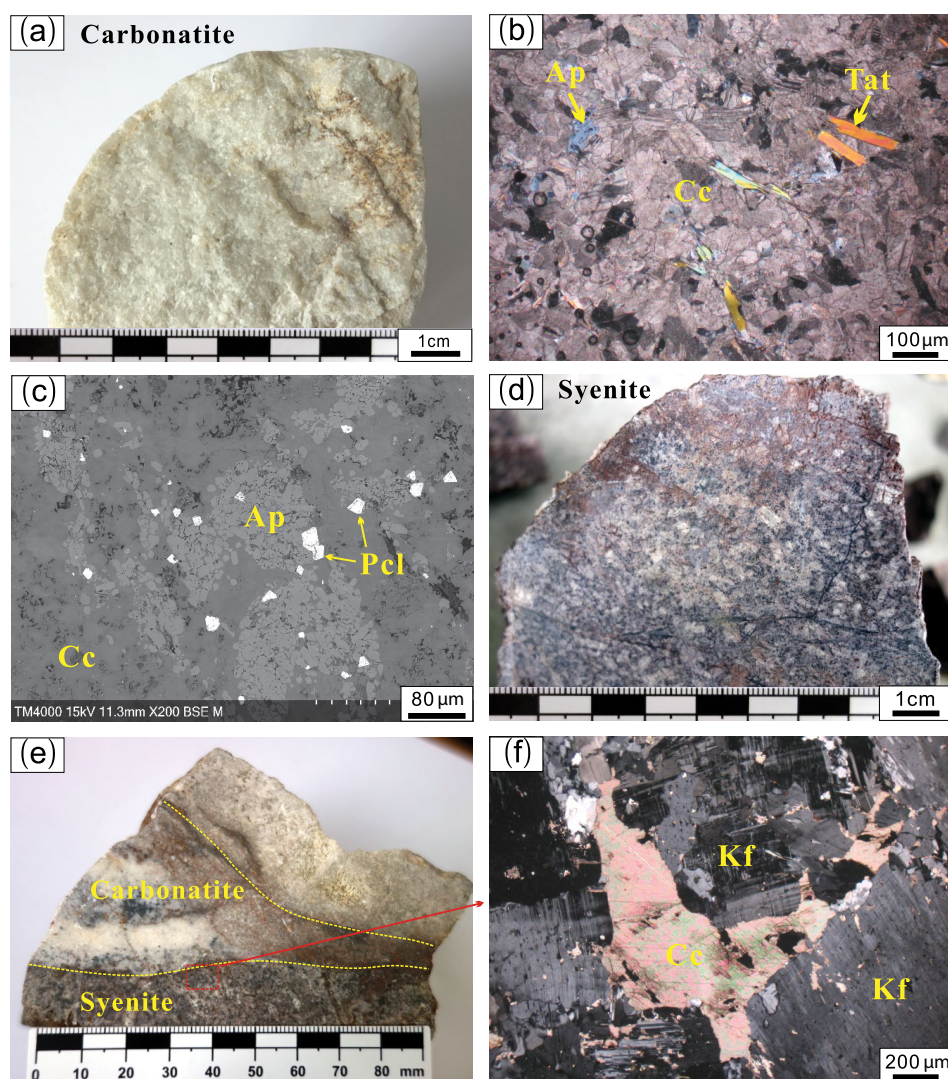

Fig. 6. (a) A carbonatite sample that is slightly overprinted by hydrothermal minerals (brown in color). (b) Photomicrograph of a representative carbonatite sample that contains calcite and minor proportions of apatite and tainiolite. (c) Backscattered electron (BSE) image of a carbonatite sample that contains abundant apatite and pyrochlore grains. (d) A syenite sample that mainly contains K-feldspar grains. (e) A sample containing both carbonatite and syenite, the boundaries of which are outlined by dotted yellow lines. (f) Photomicrograph of the rectangle area in Figure 6e, in which calcite is interstitial to K-feldspar grains. Mineral abbreviations: Ap = apatite, Cc = calcite, Kf-K = feldspar, Pcl = pyrochlore, Tat = tainiolite.
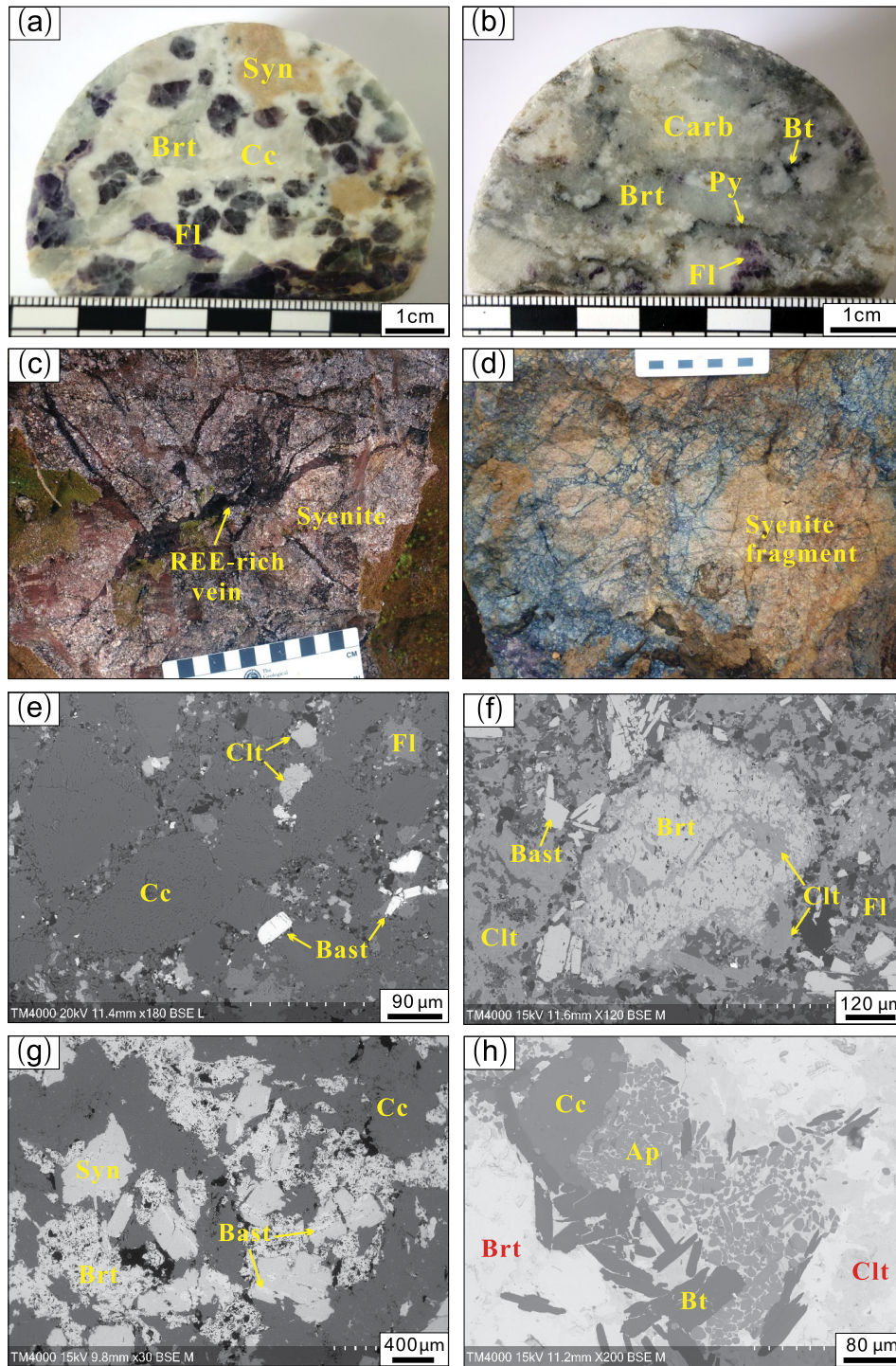
Fig. 7. (a) A massive ore sample that mainly contains calcite, fluorite, barite, and synchysite. (b) A carbonatite sample over-printed by hydrothermal veins. The vein minerals mainly include barite, fluorite, biotite, and pyrite. (c) Rare earth element (REE)-rich hydrothermal veins in a syenite sample. (d) Breccia containing angular syenite fragments that are cemented by hydrothermal minerals. (e) Backscattered electron (BSE) image of a carbonatite sample in which hydrothermal minerals (e.g., bastnäsite, fluorite, and celestite) occur interstitial to calcite grains. (f) BSE image of an ore sample that mainly contains barite, bastnäsite, fluorite, and celestite. Note that the early-stage barite is extensively overprinted by later-stage celestite. (g) BSE image of an ore sample that mainly contains barite, celestite, and calcite. Note that later-stage bastnäsite-(Ce) occurs along the rims or intracrystalline fractures of synchysite-(Ce). (h) BSE image of an ore sample that mainly contains apatite, biotite, barite, celestite, and calcite. Mineral abbreviations: Ap = apatite, Bast = bastnäsite, Brt = barite, Bt = biotite, Carb = carbonatite, Cc = calcite, Clt = celestite, Fl = fluorite, Kf = K-feldspar, Pcl = pyrochlore, Py = pyrite, Syn = synchysite, Tat = tainiolite.

Zircon U-Pb isotope dating

Zircon grains from two syenite samples (DP17-08 and DP17-47) were separated for U-Pb isotope analysis. The locations of the two samples are shown in Figure 5a. Prior to analysis, zircon was examined with cathodoluminescence (CL) imaging to reveal internal textures. The U-Pb isotope dating was conducted using a Cameca IMS-1280HR secondary ion mass spectrometer (SIMS) at the Institute of Geology and Geophysics, Chinese Academy of Sciences (IGGCAS), Beijing, China. Analytical procedures were similar to those reported by Li et al. (2010). The primary O_2^- ion beam was focused to elliptical spots with a size of 20×30 μm. Positive secondary ions were extracted with a 13-kV potential, with an intensity of approximately 8 nA. In the secondary ion beam optics, a 60-eV energy window was used, together with a mass resolution of approximately 5,400 (at 10% peak height), to separate Pb^+ peaks from isobaric interferences. An electron multiplier was used to measure secondary ion beam intensities in peak jumping mode. Measured Pb/U ratios were calibrated relative to the zircon standard TEMORA 2 ($^{206}Pb/^{238}U$ age = 416.8 ± 1.3 Ma; Black et al., 2004). Nonradiogenic Pb was subtracted from the measured Pb isotope composition using the measured ^{204}Pb. Corrections are sufficiently small to be insensitive to the choice of common Pb composition, and an average of present-day crustal composition was used. Measurements on a second zircon standard, Qinghu, were interspersed to monitor the external uncertainties. Ten analyses on the Qinghu zircon yielded a concordia age of 160.1 ± 1.5 Ma, in agreement with the recommended U-Pb age of 159.5 ± 0.2 Ma (Li et al., 2013). Uranium-Pb dating results are available in Appendix Table A2.

Bastnäsite Th-U-Pb isotope dating

Bastnäsite grains from carbonatite sample DP17-04 were used for Th-U-Pb isotope dating. The carbonatite sample was collected from drill core (borehole MJVD-20) at a depth of 92.4 m (Fig. 5b). Before analysis, transmitted- and reflected-light microscopy and backscattered electron (BSE) imaging of bastnäsite grains were used to examine inclusions, cracks, and internal textures. The analysis was performed using an Agilent 7500a quadrupole-inductively coupled plasma-mass spectrometer (Q-ICP-MS), coupled to an Analyte G2 193-nm excimer laser ablation system at IGGCAS. The analytical procedures were similar to those of Y.H. Yang et al. (2019). The analyses were performed with a spot size of 32 μm and a laser repetition rate of 6 Hz. Each spot analysis involved about 20 s of background data acquisition and 45 s of sample data acquisition. Signals of ^{202}Hg, $^{204}(Pb + Hg)$, ^{206}Pb, ^{207}Pb, ^{208}Pb, ^{232}Th, and ^{238}U were acquired, and ^{235}U was calculated from ^{238}U according to the ratio $^{238}U/^{235}U = 137.88$. The matrix-matched standard K-9 (118 ± 1 Ma) was used to correct for Th-U-Pb fractionation and instrumental mass bias. All spot analyses yielded negligible raw counts of $^{204}(Pb + Hg)$, indicating negligible common Pb. In-house bastnäsite standard LZ was used as a second standard to monitor the accuracy of the analytical procedures. Three spots yielded a weighted mean $^{208}Pb/^{232}Th$ age of 28.1 ± 0.5 Ma (2σ), which is consistent, within uncertainties, with the reported value of 28.4 ± 0.2 Ma (Ling et al., 2016). The Th-U-Pb isotope data for bastnäsite are listed in Appendix Table A3.

Major and trace element analyses of carbonatite and syenite

Carbonatite and syenite samples were crushed to powders of 200 mesh for major and trace element analyses. For major element analysis, mixtures of whole-rock powder (0.5 g) and $Li_2B_4O_7 + LiBO_2$ (5 g) were heated and fused into glass disks. The glass was analyzed by X-ray fluorescence spectroscopy at the Nanjing FocuMS Analysis Lab, China. Precisions were ±1–3% for elements in concentrations of >1 wt %, and about ±10% for elements in concentrations of <1 wt %. Loss on ignition was measured using 0.5 g of powder heated up to 1,100°C for 1 h. For trace element analyses, whole-rock powders were dissolved by distilled HNO_3 and HF. Dissolved samples were diluted to 49 mL with 1% HNO_3, and 1 mL of 500-ppb indium was added to the solution as an internal standard. Element concentrations were measured by Agilent 7700× ICP-MS at the Nanjing FocuMS Analysis Lab, China. The analytical precisions are generally better than 5% based on replicate analyses of standard samples (basalts BCR-2 and BHVO-2, andesite AGV-2, and rhyolite RGM-2, http://georem.mpch-mainz.gwdg.de). Major and trace element data are listed in Appendix Table A4.

Strontium and neodymium isotope analyses of carbonatite and syenite

For Sr and Nd isotope analyses, whole-rock powders (about 100 mg) were dissolved with HF + HNO_3 + $HClO_4$ in Teflon capsules. Chemical separation was undertaken using two-stage ion exchange procedures. First, separation of Sr and light rare earth elements (LREEs) were carried out with a cation exchange column (packed with AG50W-X12). Then, Nd was separated from LREEs using a commercial Ln Spec resin column. The Sr and Nd isotope ratios were measured on a Nu Plasma II multicollector (MC)-ICP-MS system at the Nanjing FocuMS Analysis Lab, China. Total procedural blanks were <300 pg for Sr and <100 pg for Nd. U.S. Geological Survey (USGS) reference materials BCR-2 and RGM-2 were measured to monitor the accuracy of the analytical procedures, with the following results: $^{87}Sr/^{86}Sr = 0.705004 \pm 8$ (2σ) and $^{143}Nd/^{144}Nd = 0.512635 \pm 6$ (2σ) for BCR-2 and $^{87}Sr/^{86}Sr = 0.704191 \pm 8$ (2σ) and $^{143}Nd/^{144}Nd = 0.512785 \pm 6$ (2σ) for RGM-2. These values are comparable with the reported reference values (GeoREM, http://georem.mpch-mainz.gwdg.de). In order to obtain the initial $^{87}Sr/^{86}Sr$ and $^{143}Nd/^{144}Nd$ ratios, the $^{87}Rb/^{86}Sr$ and $^{147}Sm/^{144}Nd$ ratios are required. These ratios were calculated from the concentrations of Rb, Sr, Sm, and Nd measured by ICP-MS. The Sr and Nd isotope data are listed in Appendix Table A4.

Carbon-oxygen isotope analyses of carbonatite and ore-hosting limestone

The carbon and oxygen isotope compositions of carbonatite and ore-hosting limestone were determined using an Isoprime continuous flow isotopic-ratio mass spectrometer (Elementar) at the Institute of Geochemistry, Chinese Academy of Sciences, Guiyang, China. Carbon and oxygen in carbonates were converted to CO_2 by reaction of ~10 mg carbonatite power with ~15 drops of pure phosphoric acid in sealed quartz tubes at 80°C. The extracted CO_2 was carried to the mass spectrometer by helium gas. Carbon isotope ratios are

expressed as δ notation in per mil (‰) relative to Vienna-Pee Dee Belemnite (V-PDB) and oxygen ratios to Vienna-standard mean ocean water (V-SMOW). Precisions determined through repeated analyses of reference material GBW04416 are ±0.1‰ for carbon and ±0.2‰ for oxygen. The C-O isotope data are listed in Appendix Table A5.

Oxygen isotope analysis of zircon

Oxygen isotope compositions of zircon were measured using the CAMECA IMS-1280 SIMS at IGGCAS, Beijing, following the procedures described by Li et al. (2010). A focused Cs^+ primary ion beam with an intensity of 2 nA was accelerated at 10 kV. The analytical spot size is typically 20 μm in diameter. Oxygen isotopes were measured using multicollection mode on two off-axis Faraday cups. The internal precision of a single analysis is generally better than 0.2‰ (1σ standard error) for $^{18}O/^{16}O$ ratio. Measured $^{18}O/^{16}O$ ratios were standardized to V-SMOW compositions ($^{18}O/^{16}O = 0.0020052$) and then corrected for the instrumental mass fractionation factor (IMF). The IMF was obtained using zircon standard 91500 with a $\delta^{18}O$ value of 9.9‰. A second zircon standard, Penglai, was measured to monitor the accuracy of the analytical procedure. Twenty-nine measurements of the Penglai zircon standard yielded a weighted mean $\delta^{18}O$ value of 5.31 ± 0.07‰ (2σ), which is consistent, within uncertainties, with the reported value of 5.31 ± 0.10‰ (Li et al., 2010). The zircon oxygen isotope data are listed in Appendix Table A6.

Analytical Results

Petrographic observations

Bastnäsite ($REECO_3F$) is the major REE mineral (Fig. 7e, f), with subordinate synchysite [$CaREE(CO_3)_2F$] (Fig. 7g). The major element compositions of bastnäsite and synchysite are presented in the Appendix Table A7. Barium and Sr are mainly housed in barite and celestine (Fig. 7f, g). Other hydrothermal minerals include fluorite, calcite, and strontianite, with minor amounts of quartz, apatite, biotite, and sulfide minerals (Fig. 7h). Petrographic observations show that these hydrothermal minerals were formed during two stages. The early-stage phases include synchysite, barite, calcite, and fluorite, and the late-stage phases are mainly composed of bastnäsite, celestine, strontianite, fluorite, and sulfide minerals. The early-stage synchysite is commonly overprinted by bastnäsite (Fig. 7g), and barite is overprinted by celestine (Fig. 7f).

Zircon U-Pb ages

A large proportion of zircon grains from the syenite show prismatic or dipyramid shapes, with lengths of 50–200 μm and length/width ratios of 1:1 to 2:1. These grains commonly display oscillatory zoning in cathodoluminescence (CL) images (Fig. 8a), with zoning interpreted to be magmatic in origin. There are also subordinate grains showing irregular shapes and exhibiting banded zoning in CL images (Fig. 8a). The individual CL bands vary from narrow to broad, and the contrasts between different bands may be definite to faint.

Twenty analyses were conducted on zircon crystals from sample DP17-08. The zircon grains have moderate to high U (372–2,774 ppm) and Th (346–5,792 ppm) concentrations.

Common Pb is negligible, with the f_{206} values (the proportion of common ^{206}Pb in total measured ^{206}Pb) being lower than 0.5%, apart from analysis DP17-08-07, which gave a higher f_{206} value of 3.68%. On the concordia diagram, all analyses are concordant within analytical error, and the weighted mean $^{206}Pb/^{238}U$ age is 51.6 ± 0.4 Ma ($n = 20$, mean square of weighted deviates [MSWD] = 0.7) (Fig. 8b). Seventeen analyses were conducted on zircon from sample DP17-47. The zircon grains contain 626–4,806 ppm Th and 392–2,019 ppm U. They contain low common Pb, with f_{206} values lower than 1%. All data from spot analyses are concordant and show a coherent cluster on concordia, with a weighted average $^{206}Pb/^{238}U$ age of 52.4 ± 0.4 Ma ($n = 16$, MSWD = 0.4) (Fig. 8c). Zircon grains from the two syenite samples have indistinguishable U-Pb ages, and these ages are interpreted to reflect the time of emplacement of syenite.

Bastnäsite Th-Pb ages

Bastnäsite grains from the carbonatite sample are euhedral to subhedral, with lengths of 50–500 μm (Fig. 7e). They occur in direct contact with calcite or appear as fragmented grains in the aggregates of comminuted calcite, indicating that bastnäsite was formed at the same time as, or earlier than, calcite. In BSE images, the bastnäsite grains lack visible zoning (Fig. 8d). Twenty-four Th-U-Pb isotope analyses were conducted on bastnäsite grains. The U-Pb isotope data are of poor precision due to the low contents of U (0.7–8.4 ppm), and the data are not presented and discussed in the following text. In contrast, the contents of ^{232}Th and radiogenic ^{208}Pb are high enough for precise isotopic dating. Overall, the analyses yield ^{208}Pb-^{232}Th ages ranging from 55.3 to 47.5 Ma, mostly clustered between 52.7 and 49.8 Ma (Fig. 8d). The weighted average $^{208}Pb/^{232}Th$ age is 51.4 ± 0.8 Ma ($n = 24$, MSWD = 0.6), which is consistent, within uncertainties, with the zircon U-Pb ages in this study.

Major and trace element compositions of carbonatite and syenite

Carbonatites have high contents of CaO (45.6–53.3 wt %), and low contents of MgO (<0.4 wt %), Fe_2O_3 (<0.6 wt %), and MnO (<0.7 wt %). Their SiO_2 (<1.4 wt %), Na_2O (<0.9 wt %), and K_2O (<0.2 wt %) contents are also low. The carbonatites have high and variable Sr (14,540–45,350 ppm), Ba (3,265–59,800 ppm), and REE (1,440–6,800 ppm) concentrations. The variable Sr, Ba, and REE contents are related to heterogeneous distributions of REE fluorocarbonate and Sr-Ba sulfate in the carbonatite. In the chondrite-normalized REE diagram, the carbonatites are characterized by variably LREE-rich patterns, with $(La/Yb)_N$ ratios of 46–1,367 (Fig. 9a). The carbonatites are depleted in high field strength elements (HFSEs: Nb, Ta, Zr, Hf, and Ti) and show negative anomalies in these elements on a primitive mantle-normalized trace element diagram (Fig. 9b).

Syenites have high contents of SiO_2 (60.0–62.8 wt %), K_2O + Na_2O (12.2–14.0 wt %), and Al_2O_3 (15.4–16.6 wt %) and low contents of CaO (0.2–3.3 wt %), Fe_2O_3 (2.6–4.5 wt %), and MgO (<0.3 wt %). They are characterized by high K_2O (11.6–13.6 wt %) and low Na_2O (0.3–0.6 wt %) contents, with very high K_2O/Na_2O ratios (19–51). Syenites have lower REE concentrations (270–800 ppm) than carbonatites but also display highly fractionated REE patterns, with $(La/Yb)_N$ ratios
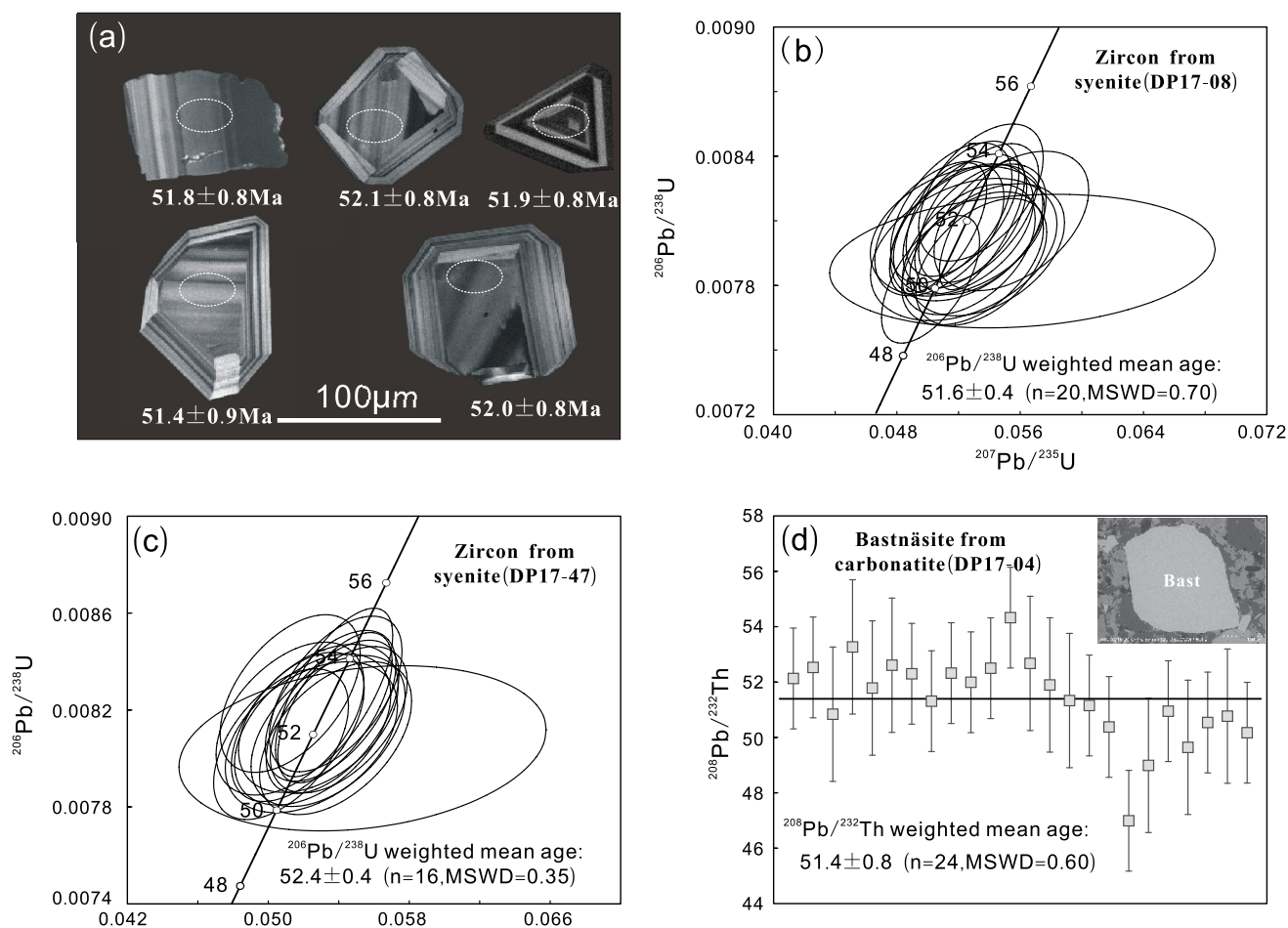
Fig. 8. (a) Cathodoluminescence image of zircon grains from the Dong Pao syenite. (b, c) Concordia diagrams showing secondary ion mass spectrometry U-Pb dating results for zircon from the Dong Pao syenite. (d) Laser ablation-inductively coupled plasma-mass spectrometry Th-Pb dating results for bastnäsite from the Dong Pao carbonatite. Bast = bastnäsite, MSWD = mean square of weighted deviates.

of 110–540 (Fig. 9c). In a primitive mantle-normalized trace element diagram, the syenite samples show variable enrichments in large ion lithophile elements (LILEs, such as Rb, Sr, Ba, and Pb) and LREEs and display depletion in HFSEs, including Nb, Ta, and Ti (Fig. 9d).

Strontium and neodymium isotope ratios of carbonatite and syenite

Carbonatites have extremely low ^{87}Rb/^{86}Sr ratios (<0.0005), and their ^{87}Sr/^{86}Sr ratios range from 0.70785 to 0.70794. They have ^{147}Sm/^{144}Nd ratios from 0.0516 to 0.1199 and ^{143}Nd/^{144}Nd ratios from 0.51227 to 0.51230.

Syenites have ^{87}Rb/^{86}Sr ratios ranging from 0.532 to 1.277, ^{87}Sr/^{86}Sr ratios from 0.70818 to 0.70840, ^{147}Sm/^{144}Nd ratios from 0.0615 to 0.0757, and ^{143}Nd/^{144}Nd ratios from 0.51226 to 0.51228. When corrected to 52 Ma, the initial ^{87}Sr/^{86}Sr ratios have a limited range of 0.70724–0.70785, and the $\varepsilon_{Nd_{(t)}}$ values range from –6.5 to –6.1 (Fig. 10).

Carbon-oxygen isotope ratios of carbonatite and ore-hosting limestone

Carbonatites have $\delta^{13}C_{V-PDB}$ values varying from –4.0 to –3.3‰ and $\delta^{18}O_{V-SMOW}$ values from 9.3 to 11.5‰ (Fig. 11).

Compared with carbonatites, the ore-hosting limestones have considerably higher $\delta^{13}C_{V-PDB}$ (–0.2 to 0.2‰) and $\delta^{18}O_{V-SMOW}$ (17.3–18.4‰) values and, as expected, plot close to the field of marine carbonates (Fig. 11).

Oxygen isotope ratios of zircon

Zircon grains from two syenite samples (DP17-08 and DP17-47) have $\delta^{18}O_{V-SMOW}$ values varying from 4.7 to 6.8‰ (Fig. 12), with an average value of 5.9‰. Specifically, zircon grains from the sample DP17-08 have $\delta^{18}O_{V-SMOW}$ values varying from 5.3 to 6.8‰. Those from sample DP17-47 generally have lower and more scattered $\delta^{18}O_{V-SMOW}$ values (4.7–6.8‰), but most values cluster in the range of 5.0–5.6‰.

Discussion

Derivation of the Dong Pao carbonatite-syenite complex from an enriched subcontinental lithospheric mantle

Zircon U-Pb dating results show that the Dong Pao syenite was emplaced at 52.4–51.6 Ma. Dated bastnäsite grains from carbonatite indicate that it was emplaced at 51.4 Ma. Thus, the carbonatite and syenite were essentially contemporaneous at ca. 52 Ma and have almost indistinguishable (^{87}Sr/^{86}Sr)$_i$
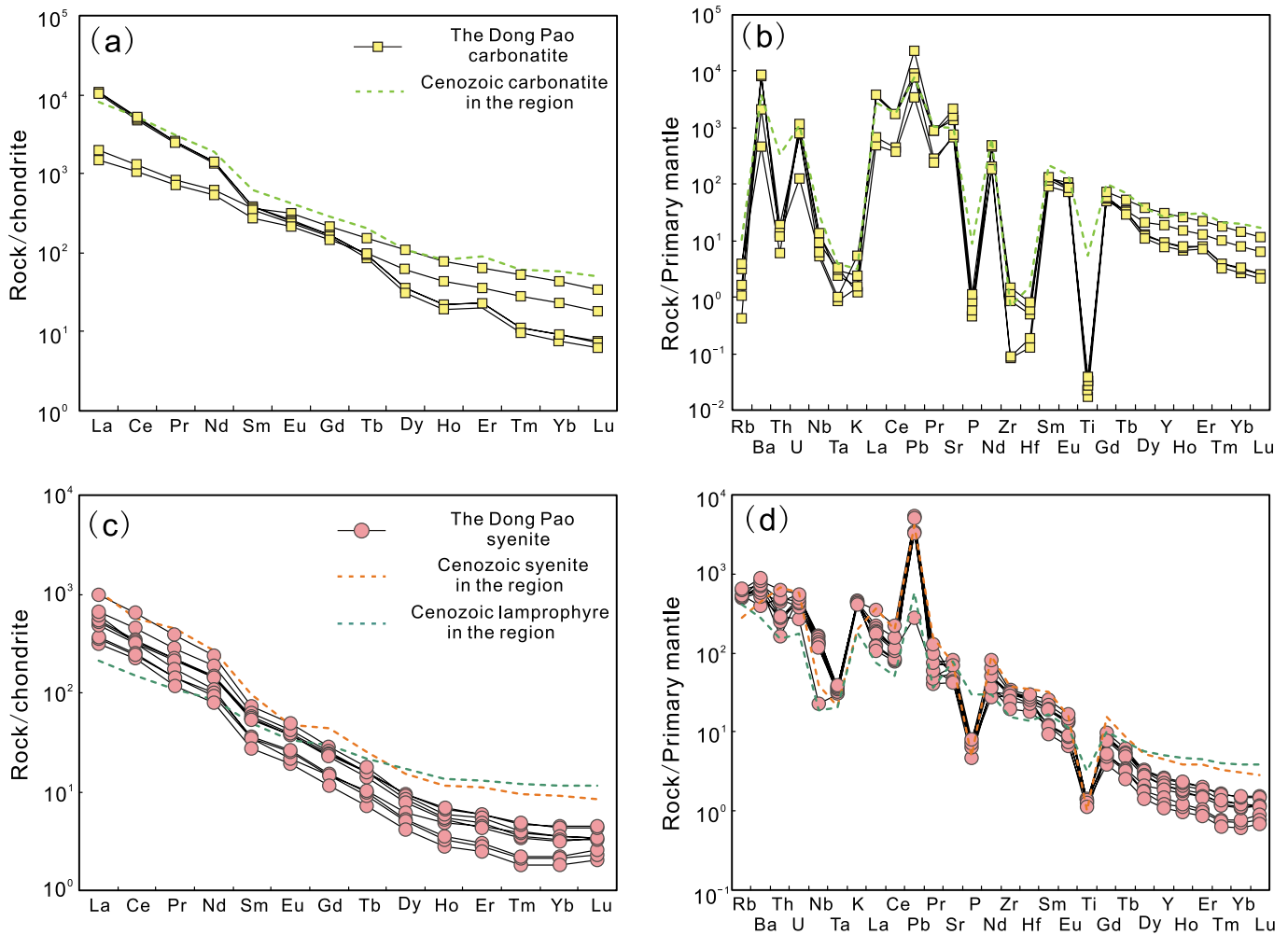
Fig. 9. (a, b) Chondrite-normalized rare earth element (REE) pattern and primitive mantle-normalized trace element pattern, respectively, for the Dong Pao carbonatite. (c, d) Chondrite-normalized REE pattern and primitive mantle-normalized trace element pattern, respectively, for the Dong Pao syenite. The average data pattern for Cenozoic lamprophyre (Yang et al., 2013) and other carbonatite complexes (Hou et al., 2015) on the west margin of the Yangtze block are also shown for comparison. The chondrite and primitive mantle values are from Sun and McDonough (1989).

and $\varepsilon_{Nd(t\,=\,52\,Ma)}$ values (Fig. 10), consistent with their derivation from a common source of CO_2-rich silicate magma. Cogenetic carbonatite and syenite can be generated through either liquid immiscibility or fractional crystallization of CO_2-rich silicate magma (Lee and Wyllie, 1998; Mitchell, 2005). Textures indicative of liquid immiscibility, such as carbonate-rich globules within a silicate matrix (Mitchell and Dawson, 2012; Pirajno et al., 2014), are not recorded in the rocks of the Dong Pao complex. Rather, where calcite and K-feldspar coexist, the former is commonly interstitial to the latter (Fig. 6f), indicative of later crystallization of carbonate. Thus, the calcite carbonatite represents a late-crystallizing phase from the CO_2-rich silicate magma.

It has been proposed that carbonatitic-alkaline rocks can be generated through partial melting of crustal components (Stepanov et al., 2016; Hegner et al., 2020; Wang et al., 2021; Wu et al., 2022). The crust-derived carbonatitic-alkaline rocks commonly have C and O isotopes closely approaching those of sedimentary carbonate rocks (Hegner et al., 2020;

Wang et al., 2020; Wu et al., 2022). However, the Dong Pao carbonatite has C-O isotope compositions that contrast with those of sedimentary carbonates but approach, but deviate slightly from, those of primary igneous carbonatite (Fig. 11). This slight deviation may indicate isotopic reequilibration of carbonatite emplaced in carbonate sedimentary rocks with crustal fluids enriched in CO_2 (Chakhmouradian et al., 2015). It is also noted that zircon grains from the Dong Pao syenite have $\delta^{18}O_{V-SMOW}$ values (5.9‰ on avg) most similar to mantle oxygen signatures (5.3 ± 0.3‰; Valley et al., 2005) but contrast with those of the crust-derived syenite in the region (Fig. 12). Thus, the Dong Pao carbonatite-syenite complex cannot be derived from partial melting of crustal rock but, as proposed more generally by many researchers, was largely derived from the mantle (Mitchell, 2005; Hou et al., 2006; Poletti et al., 2016). The Dong Pao carbonatite-syenite complex is characterized by a depletion in HFSEs and has high initial $^{87}Sr/^{86}Sr$ and low $\varepsilon_{Nd(t)}$ values (Figs. 9, 10). Depletion in HFSEs and enriched Sr-Nd isotope compositions are
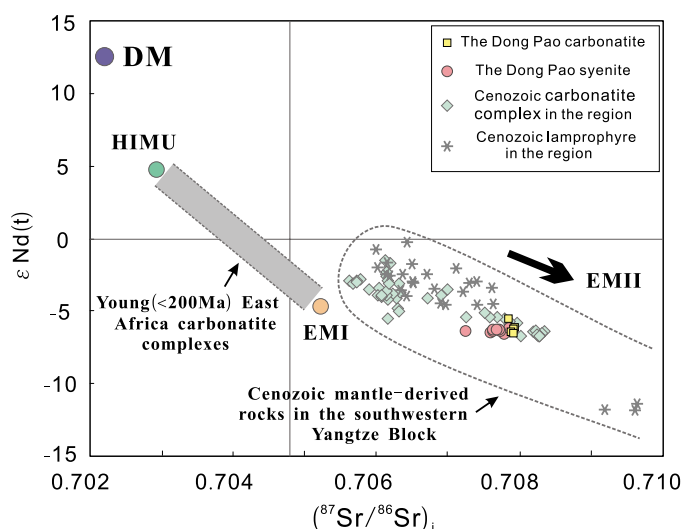
Fig. 10. $(^{87}Sr/^{86}Sr)_i$ versus $\varepsilon_{Nd(t)}$ for the Dong Pao carbonatite and syenite. The isotopic data for Cenozoic lamprophyre (Guo et al., 2005; Yang et al., 2013) and other carbonatite complexes (Maoniuping, Dalucao, and Lizhuang, Hou et al., 2015; Nam Xe, Thi et al., 2014) on the western margin of the Yangtze block are also plotted. Depleted mantle (DM), high μ value mantle (HIMU), enriched mantle-I (EMI), and enriched mantle-II (EMII) are end-member mantle components (Griffin et al., 2013). Note that the sources for the carbonatite complex and lamprophyre in the western Yangtze block are mainly EMII mantle components, whereas the sources for the young carbonatite complexes (<200 Ma) in East Africa are primarily a mixture of HIMU and EMI mantle components (Bell and Simonetti, 2010).

Fig. 11. $\delta^{13}C$ versus $\delta^{18}O$ correlation diagram for carbonatite and ore-hosting limestone in the Dong Pao deposit. The compositional fields of primary igneous carbonatite (PIC) (as defined by Taylor et al., 1967, and Demeny et al., 2004) are also shown for comparison. V-PDB = Vienna-Pee Dee Belemnite, V-SMOW = Vienna-standard mean ocean water.

inconsistent with asthenosphere-derived rocks, such as mid-ocean ridge basalts and most ocean island basalts (Hofmann, 2014), but are similar to many rocks derived from mantle lithosphere (Nelson et al., 1986; Turner et al., 1996; Pandey et al., 2017). In particular, the Dong Pao complex has geochemical and isotopic compositions that are very similar to the Cenozoic lamprophyre in the same region (Figs. 9, 10), which originated from fluid-enriched metasomatized lithospheric mantle (Guo et al., 2005). The geochemical and isotopic evidence in combination therefore suggest that the Dong Pao carbonatite-syenite complex was derived from subcontinental lithospheric mantle (SCLM) that was fertilized by REE- and CO_2-bearing fluids.

It is well established that there was long-lived Neoproterozoic (ca. 870–730 Ma) oceanic plate subduction along the western margin of the Yangtze block (Sun et al., 2009; Gao et al., 2016). From this study, the depleted mantle model age (T_{DM}) for the Dong Pao carbonatite-syenite complex has a range from 1411 to 802 Ma, mostly clustered between 970 and 802 Ma (App. Table A4). The broad coincidence of younger T_{DM} ages of the carbonatite-syenite complex with the Neoproterozoic subduction event implies that enrichment of SCLM was caused by metasomatism related to Neoproterozoic subduction. A similar explanation is also reached for the carbonatite-(alkaline) complexes in southwestern China (Hou et al., 2015; Tian et al., 2015; Liu and Hou, 2017), and, importantly, metasomatism of SCLM on the western margin of the Yangtze block by Neoproterozoic subduction is also implicated from studies of porphyry-skarn gold (Deng et al., 2015) and orogenic gold deposits (Yang et al., 2021) from the Tibetan Plateau directly along strike from Dong Pao (Fig. 2).
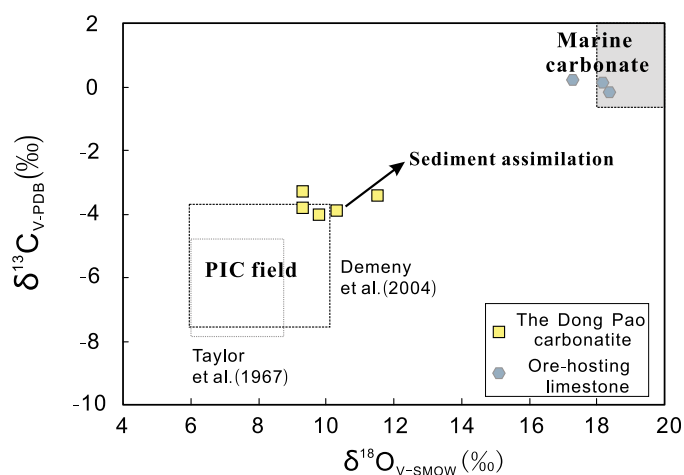
Reactivation of the Indochina-South China suture and generation of the Dong Pao REE deposit

The genesis of the Dong Pao REE-fertile carbonatite-syenite complex at ca. 52–51 Ma is enigmatic, as there is limited evidence for early Eocene magmatism or tectonic activity in northwestern Vietnam. The only other ca. 50 Ma age in the region is from the Ban Xeo A-type granite (Pham et al., 2020), which is located approximately 50 km north of the Dong Pao complex (Fig. 4). As India-Asia collision was the most prominent Cenozoic tectonic event affecting northwestern Vietnam, formation of these rare intrusions was logically related to this event.

Since the initial India-Asia collision in the early Eocene, the Tibetan Plateau has experienced uplift and intense north-south crustal shortening to accommodate the India-Asia convergence (Li et al., 2015, and references therein). Available data indicate that widespread deformation occurred over the whole plateau shortly after the onset of India-Asia collision. Apart from the Himalayan fold-and-thrust belt bounding the collision front (Guillot et al., 2003; DeCelles et al., 2014), a growing body of studies has documented deformation in the Qiangtang terrane of Central Tibet in the early Eocene. For example, activation of the Fenghuoshan fold-and-thrust belt (Fig. 13a), located in the Hoh Xil basin, could have been initiated as early as 48 Ma (Staisch et al., 2016). Moreover, the Hoh Xil basin experienced a rapid sediment accumulation at ca. 54 Ma, which corresponded to plateau uplift and enhanced erosion (Jin et al., 2018). In northern Tibet, a series of thrust and strike-slip faults (Fig. 13a), such as the Main Pamir-West Kunlun thrust belt, the western Qinling thrust fault, and the left-lateral Altyn Tagh fault, were initiated around 50–45 Ma (Yin et al., 2002; Clark et al., 2010; Cao et al., 2013). This early Eocene deformation is also supported by sedimentary records from the Qaidam basin and Tarim basin (Fig. 13a), which show initial deposition of coarse-grained sediments in high-energy environments in the early Eocene (Ji et al., 2017, and references therein).
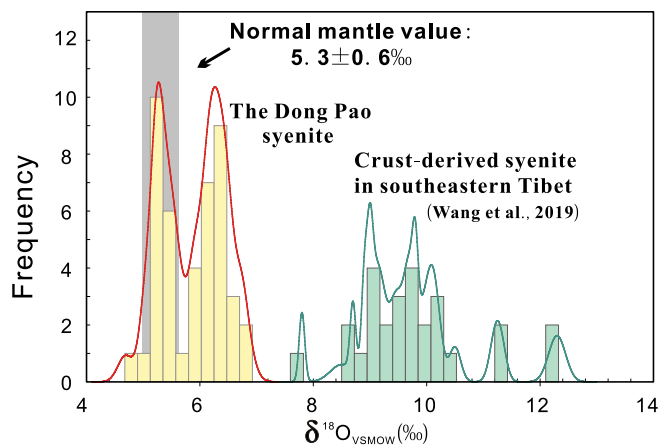
Fig. 12. Stacked histogram showing the in situ $\delta^{18}O$ values for zircon from the Dong Pao syenite. The oxygen isotope signatures for the mantle (Valley et al., 2005) and a crust-derived syenite in the eastern Tibet Plateau (Wang et al., 2019) are also shown for comparison. V-SMOW = Vienna-standard mean ocean water.

In eastern and southeastern Tibet, a significant component of India-Asia convergence was accommodated by strike-slip faulting, block rotation, and extrusion of the Indochina Peninsula. It has been well recognized that these tectonic activities peaked in the Oligocene-Miocene (Wang et al., 2006; Tang et al., 2013; Kornfeld et al., 2014). However, recent paleomagnetic studies show that block rotation started as early as the early Eocene. For example, a high-resolution magnetostratigraphic study demonstrated that the Gonjo basin (Fig. 13a) in eastern Tibet experienced an ~30° clockwise rotation relative to South China between 52 and 48 Ma (Li et al., 2020). Integration of paleomagnetic data sets obtained from Jurassic and younger rocks of the Indochina and South China blocks also reveal a clockwise rotation of northwestern Indochina relative to South China since ca. 50 Ma (Li et al., 2017). Initiation of the clockwise rotation from the early Eocene may be attributed to the regionally distributed right-lateral shear between the shortening Tibetan Plateau and rigid South China block (England and Molnar, 1990). Moreover, low-temperature thermochronology suggests that some large-scale thrust faults, such as the Lidian-Zhonghejiang fault (Fig. 13a), were initiated at ca. 50 Ma along the suture between northwestern Indochina and South China (Cao et al., 2021). All evidence of geologic activity indicates that strain was transmitted to the southeastern margin of the Tibetan Plateau shortly after the onset of the India-Asia collision, causing reorganization of lithospheric plates and local reactivation of the Indochina-South China suture (Fig. 13b). This may have led to disturbance of the mantle lithosphere on the western margin of the Yangtze block. As carbonatite melts form near the solidus of carbonated peridotites, a tectonic perturbation in the mantle has the potential to trigger low-degree partial melting to produce carbonatitic magma (Tappe et al., 2014, 2017).

It has been proposed that differential block rotation and fault activation can also cause local extension, facilitating consequent ascent and emplacement of ore-fertile magmas and fluids (Deng et al., 2021). As the Dong Pao carbonatite complex was emplaced adjacent to the suture between northwestern Indochina and South China, local reactivation of the

paleosuture had the potential to generate a tectonic disturbance of the lithospheric mantle and create local extensional/transtensional environments. Such an extensional environment at Dong Pao is indicated by the broadly northeast-southwest elongation of the syenite-carbonatite complex (Fig. 5a) at a high angle to the belt-defining sutures and major shear zones. The NE-SW–elongated complex would have been emplaced into northwest-southeast dilation zones representing the orientation of principal minimum stress during broadly NE-directed compression. An overall model for the emplacement of the Dong Pao syenite-carbonatite complex based on the interpretation of generation of a local extensional/transtensional structural environment is shown in Figure 13b. Similar scenarios have been recorded for the Gifford Creek and Cummins Range carbonatite complexes in Australia, which were generated due to intracontinental fault reactivation that was driven by far-field stresses related to supercontinent breakup or assembly (Downes et al., 2016; Slezak and Spandler, 2019).

Favorable conditions for the formation of carbonatite-related REE deposits in continental collisional belts

The India-Asia collisional belt is the best global example of a collisional orogen that hosts a series of large carbonatite-related REE deposits. Three episodes of REE mineralization can be indentified in this belt (Fig. 3), as represented by the early Eocene Dong Pao deposit (ca. 52 Ma), the Oligocene Maoniuping, Lizhuang, Muluozhai, and Nam Xe deposits (ca. 30–26 Ma), and the late Miocene Dalucao deposit (ca. 11 Ma). Although generated during different stages of collisional tectonics, these deposits share several common features.

First, all ore-hosting alkaline complexes and related ores show obvious enrichments in LREEs, Ba, and Sr and depletions in HFSEs. Moreover, the ore-hosting carbonatite-bearing complexes display Sr-Nd isotope signatures approaching the enriched mantle-II (EMII) mantle components, which are different from asthenosphere-derived carbonatites (Fig. 10). As discussed above, these geochemical features indicate that the REE-rich magmas were derived from a fertilized lithospheric mantle source related to suprasubduction metasomatism. Similar metasomatic enrichments have been identified in the mantle sources of many other REE-fertile carbonatites, such as the Weishan (Wang et al., 2020) and Miaoya (Xu et al., 2014) carbonatite complexes in China, the Hongcheon carbonatite in Korea (Kim et al., 2016), and the Palabora carbonatite in South Africa (Bolhar et al., 2020). Thus, externally driven enrichment of older mantle lithosphere in metals and volatiles is likely an important precursor process for the generation of REE-rich magmas.

It is also noteworthy that all the Cenozoic REE deposits are situated along the periphery of the India-Asia collisional belt, far from the continent-continent collision front (Fig. 2). The convergent margin is commonly associated with slab dehydration and/or asthenosphere upwelling (Griffin et al., 2013; Zhu et al., 2015), which would lead to high degree melting of mantle rocks to produce magmas with low REE fertility. Since REE- and CO_2-rich melts occur near the solidus of volatile-fluxed peridotites, excess mantle heat may be unnecessary for their formation (Tappe et al., 2014, 2017; Downes et al., 2016), and tectonic nudges of the lithosphere appear
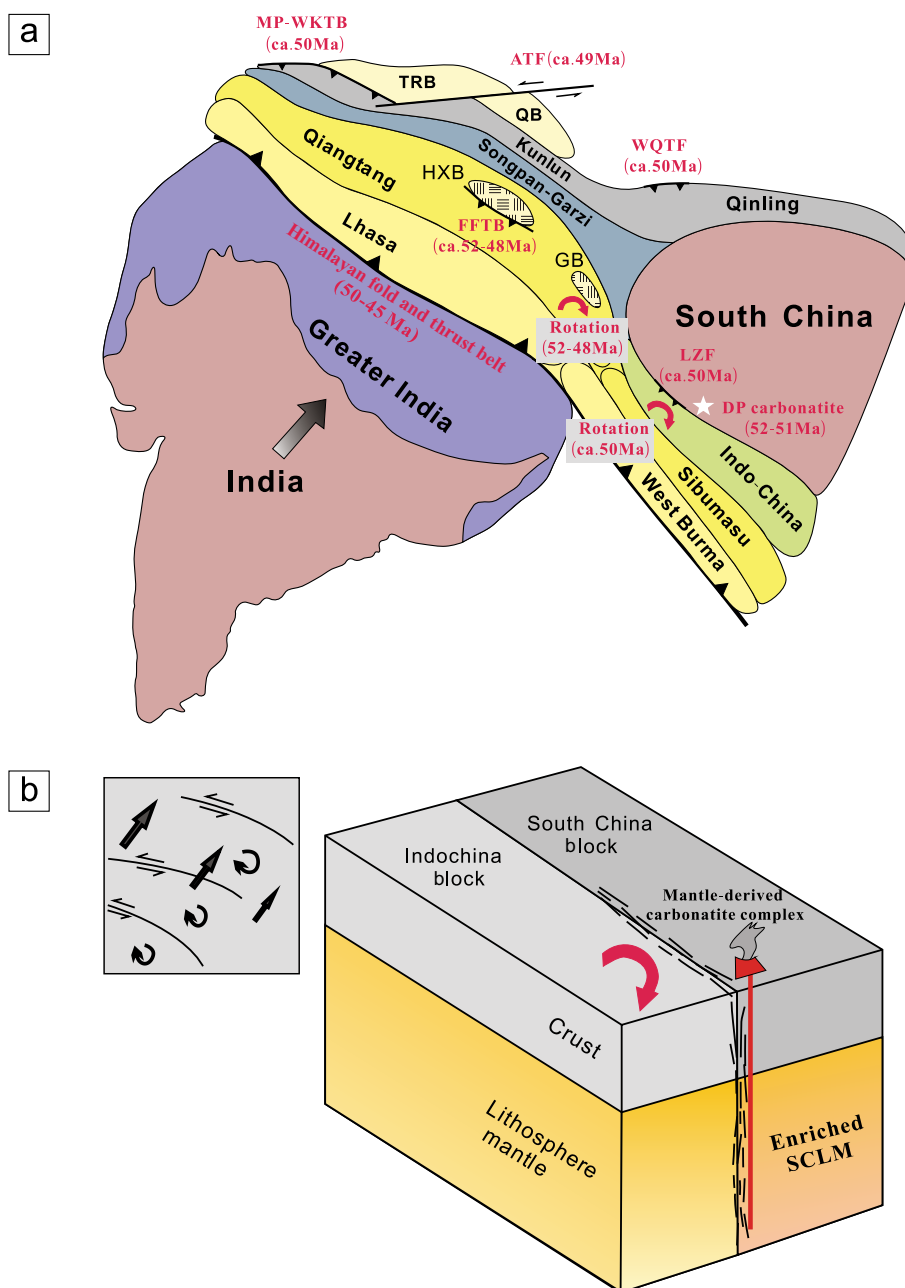
Fig. 13. (a) Early Eocene tectonic activities across the Tibet Plateau (after Cao et al., 2021). Abbreviations: Basins: GB = Gonjo basin, HXB = Hoh Xil basin, QB = Qaidam basin, TRB = Tarim basin. Faults: ATF = Altyn Tagh fault, FFTB = Fenghuoshan fold-and-thrust belt, LZF = Ludian-Zhonghejiang fault, MP-WKTB = Main Pamir-West Kunlun thrust belt, WQTF = West Qinling thrust fault. The initial timing for major faults and block rotation is labeled: Main Pamir-West Kunlun thrust belt at ca. 50–46 Ma (Yin et al., 2002; Cao et al., 2013); West Qinling thrust fault at ca. 50–45 Ma (Clark et al., 2010); Himalayan fold-and-thrust belt at ca. 50–45 Ma (Guillot et al., 2003; DeCelles et al., 2014); Altyn Tagh fault at ca. 49 Ma (Yin et al., 2002); Fenghuoshan fold-and-thrust belt at ca. 48 Ma (Staisch et al., 2016); rotation of the Gonjo basin (52–48 Ma; Li et al., 2020); rotation of northwestern Indochina (Simao basin) (~50 Ma; Li et al., 2017). (b) A model showing local reactivation of the Indochina-South China suture and generation of the mantle-derived carbonatite complex. The upper left figure shows inferred velocity field and tectonic activity in the region (according to England and Molnar, 1990). SCLM = subcontinental lithospheric mantle.

more favorable for generation of REE- and CO_2-rich melts (Woolley and Bailey, 2012; Spandler et al., 2020). During continent-continent collision, mantle lithosphere distal to the active collision front can be tectonically disturbed, facilitating the generation of low-degree partial melts at different stages of continent convergence. As illustrated by this study, this occurred at least three times during India-Asia convergence and subsequent reactivation of collision-related regional structures. Therefore, some form of tectonic disturbance of an enriched mantle lithosphere distal to a collision front is

favored for the generation of carbonatitic magmas and associated REE deposits.

Implications for future exploration of carbonatite-related REE deposits

As illustrated by this study, the carbonatite-related REE deposits were formed over a time span of about 40 m.y. in the India-Asia collision zone. Generation of these deposits was closely associated with the tectonic evolution—and particularly with changes in kinematics of major structures—in the region. Since the collision of India with Asia, the Tibetan Plateau and adjacent regions have experienced three principal stages of structural modification, namely the main-collision (ca. 60–40 Ma), late-collision (ca. 40–20 Ma), and postcollision (ca. 20 Ma to present) stages (Hou and Cook, 2009). The main-collision stage is dominated by a compressional regime with crustal shortening and thickening and synpeak metamorphism (Yin and Harrison, 2000; Aikman et al., 2008; Ding et al., 2016). The late-collision stage evolved to a transpressional to transtensional regime with strike-slip faulting, shearing, and block rotation and extrusion (Leloup et al., 1995; Wang et al., 2006; Li et al., 2017). In contrast, the postcollision stage is characterized by an extensional regime with normal fault zones at shallow crustal levels (Burchfiel et al., 1992; Blisniuk et al., 2001). Geologic and geochronological studies demonstrated that the REE deposits related to carbonatite-alkaline intrusions in southwestern China were controlled by strike-slip faulting and resultant extensional structures at the late-/postcollision stages (Hou et al., 2009). Rare magmatic rocks and deposits were formed in the main-collision epoch in southwestern China and northwestern Vietnam. The REE deposits in northwestern Vietnam were previously assumed to have formed in the late-collision stage (ca. 42–35 Ma; Tran et al., 2016), as in southwestern China. However, this geochronological study, using robust methods to produce reliable results, relates the Dong Pao REE deposit to the earlier Eocene main-collision stage of tectonic evolution. As illustrated above, far-field stresses related to India-Asia collision initiated local transtensional/extensional environments that provided dilation zones at high angles to the tectonic grain of the Tibetan orogenic belt as defined by bounding sutures. These localized extensional zones are interpreted to have facilitated carbonatite magma release from lithospheric mantle and emplacement in these zones in the crust. These localized extensional environments within an overall compressional stress regime represent potential new exploration areas to target large carbonatite-related REE deposits in the India-Asia collision zone.

In a broader extent, the most favorable exploration areas for carbonatites and related deposits are intracratonic rift, plume-related environments, or postcollisional orogens (Woolley and Kjarsgaard, 2008). The search for carbonatites in syncollisional orogenic settings is not favored from current knowledge and statistical analysis. However, this study demonstrates that such carbonatite complexes do exist and can be associated with high-tonnage REE deposits. It is significant that similar carbonatite-alkaline intrusions have been documented from contractional orogenic settings in other locations, such as the ca. 1.0 Ga Cummins Range carbonatite complex in Australia (Downes et al., 2016) and the ca. 1.4 Ga REE-rich carbonatite-alkaline complex at Mountain Pass, North America

(Poletti et al., 2016). For target generation, it is important to recognize potential dilation zones oblique to the frontal faults in structural studies of syncollisional orogenic settings elsewhere on the planet.

Conclusions

Dong Pao is a large, early Eocene (ca. 52–51 Ma) REE deposit formed on the southeastern India-Asia collision zone. The REE mineralization is genetically related to a carbonatite-syenite complex that was emplaced adjacent to the ancient Indochina-South China plate suture. The ore-hosting carbonatite-syenite complex was derived from SCLM, which had been previously metasomatized by REE- and CO_2-rich fluids. Generation of the Dong Pao complex was related to local reactivation of the Indochina-South China suture, which was induced by far-field stresses related to India-Asia collision. Related tectonic activity involving block rotation and oblique-slip faulting resulted in local transtensional environments into which the syenite-carbonatite complex was emplaced.

This study demonstrates that carbonatite-related REE deposits can form in a collisional belt, even during the period of continent-continent convergence, provided localized dilational environments oblique to major terrane trends can develop related to reactivation of lithosphere-scale sutures. Long-lived metasomatized and fertilized SCLM adjacent to craton or block margins provides both a suitable geodynamic setting and a fertile source of REE deposits. Domains where there is a conjunction of these tectonic factors provide potential new exploration areas outside normally targeted environments.

Acknowledgments

REFERENCES

Aikman, A.B., Harrison, T.M., and Ding, L., 2008, Evidence for early (>44 Ma) Himalayan crustal thickening, Tethyan Himalaya, southeastern Tibet: Earth and Planetary Science Letters, v. 274, p. 14–23.

Aitchison, J.C., Abrajevitch, A., Ali, J.R., Badengzhu, Davis, A.M., Luo, H., Liu, J.B., McDermid, I.R.C., and Ziabrev, S., 2002, New insights into the evolution of the Yarlung Tsangpo suture zone, Xizang (Tibet), China: Episodes, v. 25, p. 90–94.

Bell, K., and Simonetti, A., 2010, Source of parental melts to carbonatites—critical isotopic constraints: Mineralogy and Petrology, v. 98, p. 77–89.

Bell, K., Kjarsgaard, B.A., and Simonetti, A., 1998, Carbonatites—into the twenty-first century: Journal of Petrology, v. 39, p. 1839–1845.

Bian, W., Yang, T., Peng, W., Wang, S., Gao, F., Zhang, S., Wu, H., Li, H., Cao, L., Jiang, T., and Wang, H., 2021, Paleomagnetic constraints on the India-Asia collision and the size of Greater India: Journal of Geophysical Research: Solid Earth, v. 126, article e2021JB021965.

Bierlein, F.P., Groves, D.I., and Cawood, P.A., 2009, Metallogeny of accretionary orogens—the connection between lithospheric processes and metal endowment: Ore Geology Reviews, v. 36, p. 282–292.

Black, L.P., Kamo, S.L., Allen, C.M., Davis, D.W., Aleinikoff, J.N., Valley, J.W., Mundil, R., Campbell, I.H., Korsch, R.J., Williams, I.S., and Foudoulis, C.,

2004, Improved $^{206}Pb/^{238}U$ microprobe geochronology by the monitoring of a trace-element-related matrix effect; SHRIMP, ID-TIMS, ELA-ICP-MS and oxygen isotope documentation for a series of zircon standards: Chemical Geology, v. 205, p. 115–140.

Blisniuk, P.M., Hacker, B., Glodny, J., Ratschbacher, L., Bill, S., Wu, Z.H., McWilliams, M.O., and Calvert, A., 2001, Normal faulting in central Tibet since at least 13.5 Myr ago: Nature, v. 412, p. 628–632.

Bolhar, R., Whitehouse, M.J., Milani, L., Magalhaes, N., Golding, S.D., Bybee, G., LeBras, L., and Bekker, A., 2020, Atmospheric S and lithospheric Pb in sulphides from the 2.06 Ga Phalaborwa phoscorite-carbonatite complex, South Africa: Earth and Planetary Science Letters, v. 530, article 115939.

Burchfiel, B.C., Chen, Z., Hodges, K.V., Liu, Y., Royden, L.H., Deng, C., and Xu, J., 1992, The south Tibetan detachment system, Himalayan orogen: Extension contemporaneous with and parallel to shortening in a collisional mountain belt: Geological Society of America, Special Paper 269, p. 1–41.

Cao, K., Wang, G., van der Beek, P., Bernet, M., and Zhang, K., 2013, Cenozoic thermo-tectonic evolution of the northeastern Pamir revealed by zircon and apatite fission-track thermochronology: Tectonophysics, v. 589, p. 17–32.

Cao, K., Leloup, P.H., Wang, G., Liu, W., Maheo, G., Shen, T., Xu, Y., Sorel, P., and Zhang, K., 2021, Thrusting, exhumation, and basin fill on the western margin of the South China block during the India-Asia collision: Geological Society of America Bulletin, v. 133, p. 74–90.

Chakhmouradian, A.R., and Wall, F., 2012, Rare earth elements: Minerals, mines, magnets (and more): Elements, v. 8, p. 333–340.

Chakhmouradian, A.R., Mumin, A.H., Demény, A., and Elliott, B., 2008, Postorogenic carbonatites at Eden Lake, Trans-Hudson orogen (northern Manitoba, Canada): Geological setting, mineralogy and geochemistry: Lithos, v. 103, p. 503–526.

Chakhmouradian, A.R., Reguir, E.P., Kressall, R.D., Crozier, J., Pisiak, L.K., Sidhu, R., and Yang, P., 2015, Carbonatite-hosted niobium deposit at Aley, northern British Columbia (Canada): Mineralogy, geochemistry and petrogenesis: Ore Geology Reviews, v. 64, p. 642–666.

Chandra, J., Paul, D., Stracke, A., Chabaux, F., and Granet, M., 2019, The origin of carbonatites from Amba Dongar within the Deccan large igneous province: Journal of Petrology, v. 60, p. 1119–1134.

Chung, S.L., Lee, T.Y., Lo, C.H., Wang, P.L., Chung, S.L., Yem, N.T., Hoa, T.T., and Genyao, W., 1997, Intraplate extension prior to continental extrusion along the Ailao Shan-Red River shear zone: Geology, v. 25, p. 311–314.

Clark, M.K., Farley, K.A., Zheng, D., Wang, Z., and Duvall, A.R., 2010, Early Cenozoic faulting of the northern Tibetan Plateau margin from apatite (U-Th)/He ages: Earth and Planetary Science Letters, v. 296, no. 1–2, p. 78–88.

Dalton, J.A., and Wood, B.J., 1993, The compositions of primary carbonate melts and their evolution through wallrock reaction in the mantle: Earth and Planetary Science Letters, v. 119, p. 511–525.

DeCelles, P., Kapp, P., Gehrels, G., and Ding, L., 2014, Paleocene-Eocene foreland basin evolution in the Himalaya of southern Tibet and Nepal: Implications for the age of initial India-Asia collision: Tectonics, v. 33, no. 5, p. 824–849.

Demény, A., Sitnikova, M., and Karchevsky, P., 2004, Stable C and O isotope compositions of carbonatite complexes of the Kola alkaline province: Phoscorite-carbonatite relationships and source compositions, in Wall, F., and Zaitsev, A., eds., Phoscorites and carbonatites from mantle to mine: The key example of the Kola alkaline province: Cambridge, Black Bear Press, p. 407–432.

Deng, J., Wang, Q., and Li, G., 2015, Geology and genesis of the giant Beiya porphyry-skarn gold deposit northwestern Yangtze block China: Ore Geology Reviews, v. 70, p. 457–485.

Deng, J., Wang, Q., Gao, L., He, W., Yang, Z., Zhang, S., Chang, L., Li, G., Sun, X., and Zhou, D., 2021, Differential crustal rotation and its control on giant ore clusters along the eastern margin of Tibet: Geology, v. 49, p. 428–432.

Ding, H., Zhang, Z., Dong, X., Tian, Z., Xiang, H., Mu, H., Guo, Z., Shui, X., Li, W., and Mao, L., 2016, Early Eocene (ca. 50 Ma) collision of the Indian and Asian continents: Constraints from the North Himalayan metamorphic rocks, southeastern Tibet: Earth and Planetary Science Letters, v. 435, p. 64–73.

Ding, L., Maksatbek, S., Cai, F., Wang, H.Q., Song, P.P., Ji, W.Q., Xu, Q., Zhang, L.Y., Muhammad, Q., and Upendra, B., 2017, Processes of initial collision and suturing between India and Asia: Science China—Earth Sciences, v. 60, p. 635–651.

Donaldson, D.G., Webb, A.A.G., Menold, C.A., Kylander-Clark, A.R., and Hacker, B.R., 2013, Petrochronology of Himalayan ultrahigh-pressure eclogite: Geology, v. 41, no. 8, p. 835–838.

Downes, P.J., Dunkley, D.J., Fletcher, I.R., McNaughton, N.J., Rasmussen, B., Jaques, A.L., Verrall, M., and Sweetapple, M.T., 2016, Zirconolite, zircon and monazite-(Ce) U-Th-Pb age constraints on the emplacement, deformation and alteration history of the Cummins Range carbonatite complex, Halls Creek orogen, Kimberley region, Western Australia: Mineralogy and Petrology, v. 110, p. 199–222.

Duong, V.H., Trinh, P.T., Nguyen, T.D., Piestrzyski, A., Nguyen, D.C., Pieczonka, J., Ngo, X.D., Van, P.T., Pham, B.T., Nguyen-Van, H., et al., 2021, Cu-Au mineralization of the Sin Quyen deposit in north Vietnam: A product of Cenozoic left-lateral movement along the Red River shear zone: Ore Geology Reviews, v. 132, article 104065.

England, P., and Molnar, P., 1990, Right-lateral shear and rotation as the explanation for strike-slip faulting in eastern Tibet: Nature, v. 344, p. 140–142.

Faure, M., Lepvrier, C., Nguyen, V.V., Vu, T.V., Lin, W., and Chen, Z.C., 2014, The South China block-Indochina collision: Where, when, and how?: Journal of Asian Earth Sciences, v. 79, p. 260–274.

Gao, R., Chen, C., Wang, H., Lu, Z., Brown, L., Dong, S., Feng, S., Li, Q., Li, W., Wen, Z., and Li, F., 2016, SINOPROBE deep reflection profile reveals a Neo-Proterozoic subduction zone beneath Sichuan basin: Earth and Planetary Science Letters, v. 454, p. 86–91.

Giebel, R.J., Marks, A.A.W., Gauert, C.D.K., and Markl, G., 2019, A model for the formation of carbonatite-phoscorite assemblages based on the compositional variations of mica and apatite from the Palabora carbonatite complex, South Africa: Lithos, v. 324–325, p. 89–104.

Goodenough, K.M., Schilling, J., Jonsson, E., Kalvig, P., Charles, N., Tuduri, J., Deady, E.A., Sadeghi, M., Schiellerup, H., Müller, A., et al., 2016, Europe's rare earth element resource potential: An overview of REE metallogenic provinces and their geodynamic setting: Ore Geology Reviews, v. 72, p. 838–856.

Griffin, W.L., Begg, G.C., and O'Reilly, S.Y., 2013, Continental-root control on the genesis of magmatic ore deposits: Nature Geoscience, v. 6, p. 905–910.

Groves, D.I., and Bierlein, F.P., 2007, Geodynamic settings of mineral deposit systems: Journal of the Geological Society, London, v. 164, p. 19–30.

Guillot, S., Garzanti, E., Baratoux, D., Marquer, D., Mahéo, G., and De Sigoyer, J., 2003, Reconstructing the total shortening history of the NW Himalaya: Geochemistry Geophysics Geosystems, v. 4, article 1064.

Guo, Z.F., Hertogen, J., Liu, J.Q., Pasteels, P., Boven, A., Punzalan, L., He, H.Y., Luo, X.J., and Zhang, W.H., 2005, Potassic magmatism in western Sichuan and Yunnan provinces, SE Tibet, China: Petrological and geochemical constraints on petrogenesis: Journal of Petrology, v. 46, p. 33–78.

Hegner, E., Rajesh, S., Willbold, M., Muller, D., Joachimski, M., Hofmann, M., Linnemann, U., Zieger, J., and Pradeepkumar, A.P., 2020, Sediment-derived origin of the putative Munnar carbonatite, South India: Journal of Asian Earth Sciences, v. 200, article 104432.

Hofmann, A.W., 2014, Sampling mantle heterogeneity through oceanic basalts: Isotopes and trace elements, in Holland, H.D., and Turekian, K.K. eds., Treatise on geochemistry, 2nd ed.: Elsevier, p. 119–142.

Hou, Z.Q., and Cook, N.J., 2009, Metallogenesis of the Tibetan collisional orogen: A review and introduction to the special issue: Ore Geology Reviews, v. 36, p. 2–24.

Hou, Z.Q., Tian, S.H., Yuan, Z.X., Xie, Y.L., Yin, S.P., Yi, L.S., Fei, H.C., and Yang, Z.M., 2006, The Himalayan collision zone carbonatites in western Sichuan, SW China: Petrogenesis, mantle source and tectonic implication: Earth and Planetary Science Letters, v. 244, p. 234–250.

Hou, Z.Q., Tian, S.H., Xie, Y.L., Yang, Z., Yuan, Z., Yin, S., Yi, L., Fei, H., Zou, T., Bai, G., and Li, X., 2009, The Himalayan Mianning-Dechang REE belt associated with carbonatite alkaline complexes, eastern Indo-Asian collision zone, SW China: Ore Geology Reviews, v. 36, p. 65–89.

Hou, Z.Q., Liu, Y., Tian, S.H., Yang, Z.M., and Xie, Y.L., 2015, Formation of carbonatite-related giant rare-earth-element deposits by the recycling of marine sediments: Scientific Reports, v. 5, article 10231.

Hu, X., Garzanti, E., Moore, T., and Raffi, I., 2015, Direct stratigraphic dating of India-Asia collision onset at the Selandian (middle Paleocene, 59 ± 1 Ma): Geology, v. 43, no. 10, p. 859–862.

Ji, J., Zhang, K., Clift, P., Zhuang, G., Song, B., Ke, X., and Xu, Y., 2017, High-resolution magnetostratigraphic study of the Paleogene-Neogene strata in the Northern Qaidam basin: Implications for the growth of the northeastern Tibetan Plateau: Gondwana Research, v. 46, p. 141–155.

Jin, C., Liu, Q., Liang, W., Roberts, A.P., Sun, J., Hu, P., Zhao, X., Su, Y., Jiang, Z., Liu, Z., Duan, Z., Yang, H., and Yuan, S., 2018, Magnetostratigraphy of the Fenghuoshan Group in the Hoh Xil basin and its tectonic implications for India-Eurasia collision and Tibetan Plateau deformation: Earth and Planetary Science Letters, v. 486, p. 41–53.

Kim, N., Cheong, A.C., Yi, K., Jeong, Y.J., and Koh, S.M., 2016, Post-collisional carbonatite-hosted rare earth element mineralization in the Hongcheon area, central Gyeonggi massif, Korea: Ion microprobe monazite U-Th-Pb geochronology and Nd-Sr isotope geochemistry: Ore Geology Reviews, v. 79, p. 78–87.

Kornfeld, D., Eckert, S., Appel, E., Ratschbacher, L., Pfänder, J., Liu, D., and Ding, L., 2014, Clockwise rotation of the Baoshan block due to southeastward tectonic escape of Tibetan crust since the Oligocene: Geophysical Journal International, v. 197, p. 149–163.

Lee, W-J., and Wyllie P.L., 1998, Processes of crustal carbonatite formation by liquid immiscibility and differentiation, elucidated by model systems: Journal of Petrology, v. 39, p. 2005–2013.

Leloup, P.H., Lacassin, R., Tapponnier, P., Schärer, U., Zhong, D., Liu, X., Zhang, L., Ji, S., and Trinh, P., 1995, The Ailaoshan-Red River shear zone (Yunnan, China), Tertiary transform boundary of Indochina: Tectonophysics, v. 252, p. 3–84.

Li, S., van Hinsbergen, D.J.J., Najman, Y., Liu-Zeng, J., Deng, C., and Zhu, R., 2020, Does pulsed Tibetan deformation correlate with Indian plate motion changes?: Earth and Planetary Science Letters, v. 536, article 116144.

Li, S.H., Advokaat, E.L., van Hinsbergen, D.J.J., Koymans, M., Deng, C., and Zhu, R., 2017, Paleomagnetic constraints on the Mesozoic-Cenozoic paleolatitudinal and rotational history of Indochina and South China: Review and updated kinematic reconstruction: Earth-Science Reviews, v. 171, p. 58–77.

Li, X.C., and Zhou, M.F., 2018, The nature and origin of hydrothermal REE mineralization in the Sin Quyen deposit, northwestern Vietnam: Economic Geology, v. 113, p. 645–673.

Li, X.C., Zhou, M.F., Chen, W.T., Zhao, X.F., and Tran, M.D., 2018a, Uranium-lead dating of hydrothermal zircon and monazite from the Sin Quyen Fe-Cu-REE-Au-(U) deposit, northwestern Vietnam: Mineralium Deposita, v. 53, p. 399–416.

Li, X.C., Zhao, J.H., Zhou, M.F., Gao, J.F., Sun, W.H., and Tran, M.D., 2018b, Neoproterozoic granitoids from the Phan Si Pan belt, Northwest Vietnam: Implication for the tectonic linkage between Northwest Vietnam and the Yangtze block: Precambrian Research, v. 309, p. 212–230.

Li, X.H., Li, W.X., Li, Q.L., Wang, X.C., Liu, Y., and Yang, Y.H., 2010, Petrogenesis and tectonic significance of the ~850 Ma Gangbian alkaline complex in South China: Evidence from in-situ zircon U-Pb and Hf-O isotopes and whole-rock geochemistry: Lithos, v. 114, p. 1–15.

Li, X.H., Tang, G.Q., Gong, B., Yang, Y.H., Hou, K.J., Hu, Z.C., Li, Q.L., Liu, Y., and Li, W.X., 2013, Qinghu zircon: A working reference for microbeam analysis of U-Pb age and Hf and O isotopes: Chinese Science Bulletin, v. 58, p. 4647–4654.

Li, Y., Wang, C., Dai, J., Xu, G., Hou, Y., and Li, X., 2015, Propagation of the deformation and growth of the Tibetan-Himalayan orogen: A review: Earth-Science Reviews, v. 143, p. 36–61.

Liegeois, J.P., 1998, Preface: Some words on the post-collisional magmatism: Lithos, v. 45, p. 15–17.

Ling, X.X., Li, Q.L., Liu, Y., Yang, Y.H., Liu, Y., Tang, G.Q., and Li, X.H., 2016, In-situ SIMS Th-Pb dating of bastnaesite: Constraint on the mineralization time of the Himalayan Mianning-Dechang rare earth element deposits: Journal of Analytical Atomic Spectrometry, v. 31, p. 1680–1687.

Liu, C.Z., Chung, S.-L., Wu, F.Y., Zhang, C., Xu, Y., Wang, J.G., Chen, Y., and Guo, S., 2016, Tethyan suturing in Southeast Asia: Zircon U-Pb and Hf-O isotopic constraints from Myanmar ophiolites: Geology, v. 44, no. 4, p. 311–314.

Liu, Y., and Hou, Z.Q., 2017, A synthesis of mineralization styles with an integrated genetic model of carbonatite-syenite-hosted REE deposits in the Cenozoic Mianning-Dechang REE metallogenic belt, the eastern Tibetan Plateau, southwestern China: Journal of Asian Earth Sciences, v. 137, p. 35–79.

Lu, Y.J., Kerrich, R., Kemp, A.I.S., McCuaig, T.C., Hou, Z.Q., Hart, C.J.R., Li, Z.X., Cawood, P.A., Bagas, L., Yang, Z.M., Cliff, J., Belousov, E.A., Jourdan, F., and Evans, N.J., 2013, Intracontinental Eocene-Oligocene porphyry Cu mineral systems of Yunnan, Western Yangtze craton, China: Compositional characteristics, sources, and implications for continental collision metallogeny: Economic Geology, v. 108, p. 1541–1576.

Marignac, C., and Cuney, M., 1999, Ore deposits of the French Massif Central: Insight into the metallogenesis of the Variscan collision belt: Mineralium Deposita, v. 34, p. 472–504.

Mclean, R.N., 2002, The Sin Quyen iron-oxide-copper-gold-rare earth oxide mineralization of North Vietnam, in Porter, T.M., ed., Hydrothermal iron oxide copper-gold and related deposits: A global perspective, v. 2: Adelaide, PGC Publishing, p. 293–301.

Metcalfe, I., 2013, Gondwana dispersion and Asian accretion: Tectonic and palaeogeographic evolution of eastern Tethys: Journal of Asian Earth Sciences, v. 66, p. 1–33.

Mitchell, R.H., 2005, Carbonatites and carbonatites and carbonatites: The Canadian Mineralogist, v. 43, p. 2049–2068.

Mitchell, R.H., and Dawson J.B., 2012, Carbonate-silicate immiscibility and extremely peralkaline silicate glasses from Nasira cone and recent eruptions at Oldoinyo Lengai volcano, Tanzania: Lithos, v. 152, p. 40–46.

Najman, Y., Appel, E., Boudagher-Fadel, M., Bown, P., Carter, A., Garzanti, E., Godin, L., Han, J., Liebke, U., Oliver, G., et al., 2010, Timing of India-Asia collision: Geological, biostratigraphic, and palaeomagnetic constraints: Journal of Geophysical Research: Solid Earth, v. 115, no. B12, article B12416.

Nelson, D.R., McCulloch, M.T., and Sun, S.S., 1986, The origins of ultrapotassic rocks as inferred from Sr, Nd and Pb isotopes: Geochimica Cosmochimica Acta, v. 50, p. 231–245.

Pandey, A., Rao, N.V.C., Chakrabarti, R., Pandit, D., Pankaj, P., Kumar, A., and Sahoo, S., 2017, Petrogenesis of a Mesoproterozoic shoshonitic lamprophyre dyke from the Wajrakarur kimberlite field, eastern Dharwar craton, southern India: Geochemical and Sr-Nd isotopic evidence for a modified sub-continental lithospheric mantle source: Lithos, v. 292, p. 218–233.

Pham, T.T., Shellnutt, J.G., Tran, T.A., and Lee, H.Y., 2020, Petrogenesis of Eocene to early Oligocene granitic rocks in Phan Si Pan uplift area, northwestern Vietnam: Geochemical implications for the Cenozoic crustal evolution of the South China block: Lithos, v. 372–373, article 105640.

Pirajno, F., 2015, Intracontinental anorogenic alkaline magmatism and carbonatites, associated mineral systems and the mantle plume connection: Gondwana Research, v. 27, p. 1181–1216.

Pirajno, F., González-Álvarez, I., Chen, W., Kyser, K.T., Simonetti, A., Leduc, E., and le Gras, M., 2014, The Gifford Creek ferrocarbonatite complex, Gascoyne province, Western Australia: Associated fenitic alteration and a putative link with the ~1075 Ma Warakurna LIP: Lithos, v. 202–203, p. 100–119.

Poletti, J.E., Cottle, J.M., Hagen-Peter, G.A., and Lackey J.S., 2016, Petrochronological constraints on the origin of the Mountain Pass ultrapotassic and carbonatite intrusive suite, California: Journal of Petrology, v. 57, p. 1555–1598.

Simandl, G.J., and Paradis, S., 2018, Carbonatites: Related ore deposits, resources, footprint, and exploration methods: Applied Earth Science, v. 127, p. 123–152.

Slezak, P., and Spandler, C., 2019, Carbonatites as recorders of mantle-derived magmatism and subsequent tectonic events: An example of the Gifford Creek carbonatite complex, Western Australia: Lithos, v. 328–329, p. 212–227.

Spandler, C., Slezak, P., and Nazari-Dehkordi, T., 2020, Tectonic significance of Australian rare earth element deposits: Earth-Science Reviews, v. 207, article 103219.

Staisch, L.M., Niemi, N.A., Clark, M.K., and Chang, H., 2016, Eocene to late Oligocene history of crustal shortening within the Hoh Xil basin and implications for the uplift history of the northern Tibetan Plateau: Tectonics, v. 35, no. 4, p. 862–895.

Stepanov, A.S., Hermann, J., Rubatto, D., Korsakov, A.V., and Danyushevsky, L.V., 2016, Melting history of an ultrahigh-pressure paragneiss revealed by multiphase solid inclusions in garnet, Kokchetav Massif, Kazakhstan: Journal of Petrology, v. 57, no. 8, p. 1531–1554.

Sun, S.S., and McDonough, W.F., 1989, Chemical and isotope systematics of oceanic basalts: Implications for mantle composition and processes: Geological Society of London, Special Publication 42, p. 313–345.

Sun, W.H., Zhou, M.F., Gao, J.F., Yang, Y.H., Zhao, X.F., and Zhao, J.H., 2009, Detrital zircon U-Pb geochronological and Lu-Hf isotopic constraints on the Precambrian magmatic and crustal evolution of the western Yangtze block, SW China: Precambrian Research, v. 172, p. 99–126.

Tang, Y., Liu, J.L., Tran, M.D., Song, Z., Wu, W., Zhang, Z., Zhao, Z., and Chen, W., 2013, Timing of left-lateral shearing along the Ailao Shan-Red River shear zone: Constraints from zircon U-Pb ages from granitic rocks in the shear zone along the Ailao Shan Range, Western Yunnan, China: International Journal of Earth Sciences, v. 102, p. 605–626.

Tappe, S., Kjarsgaard, B.A., Kurszlaukis, S., Nowell, G.M., and Phillips, D., 2014, Petrology and Nd-Hf isotope geochemistry of the Neoproterozoic Amon kimberlite sills, Baffin Island (Canada): Evidence for deep mantle magmatic activity linked to supercontinent cycles: Journal of Petrology, v. 55, p. 2003–2042.

Tappe, S., Brand, N.B., Strake, A., van Acken, D., Liu, C.Z., Strauss, H., Wu, F.Y., Luguet, A., and Mitchell, R.H., 2017, Plates or plumes in the origin of kimberlites: U/Pb perovskite and Sr-Nd-Hf-Os-C-O isotope constraints from the Superior craton (Canada): Chemical Geology, v. 455, p. 57–83.

Tapponnier, P., Lacassin, R., Leloup, P.H., Scharer, U., Zhong, D., Wu, H.H., Liu, X., Ji, S., Zhang, L., and Zhong, J., 1990, The Ailao Shan-Red River metamorphic belt: Tertiary left-lateral shear between Sundaland and South China: Nature, v. 343, p. 431–437.

Tapponnier, P., Xu, Z.Q., Roger, F., Meyer, B., Arnaud, N., Wittlinger, G., and Yang, J.S., 2001, Oblique stepwise rise and growth of the Tibet Plateau: Science, v. 294, no. 547, p. 1671–1677.

Taylor, H.P., Frechen, J., and Degens, E.T., 1967, Oxygen and carbon isotope studies of carbonatites from the Laacher See district, West Germany and the Alnö district, Sweden: Geochimica et Cosmochimica Acta, v. 31, p. 407–430.

Thi, T.N., Wada, H., Ishikawa, T., and Shimano, T., 2014, Geochemistry and petrogenesis of carbonatites from South Nam Xe, Lai Chau area, Northwest Vietnam: Mineralogy and Petrology, v. 108, p. 371–390.

Tian, S.H., Hou, Z.Q., Su, A., Qiu, L., Mo, X.X., Hou, K.J., Zhao, Y., Hu, W.J., and Yang, Z.S., 2015, The anomalous lithium isotopic signature of Himalayan collisional zone carbonatites in western Sichuan, SW China: Enriched mantle source and petrogenesis: Geochimica et Cosmochimica Acta, v. 159, p. 42–60.

Tran, H.T., Lan, C.Y., Usuki, T., Shellnutt, J.G., Pham, T.D., Tran, T.A., Pham, N.C., Ngo, T.P., Izokh, A.E., and Borisenko, A.S., 2015, Petrogenesis of late Permian silicic rocks of Tu Le basin and Phan Si Pan uplift (NW Vietnam) and their association with the Emeishan large igneous province: Journal of Asian Earth Sciences, v. 109, p. 1–19.

Tran, M.D., Liu, J.L., Nguyen, Q.L., Chen, Y., Tang, Y., Song, Z., Zhang, Z., and Zhao, Z., 2014, Cenozoic high-K alkaline magmatism and associated Cu-Mo-Au mineralization in the Jinping-Fan Si Pan region, southeastern Ailao Shan-Red River shear zone, southwestern China-northwestern Vietnam: Journal of Asian Earth Sciences, v. 79, p. 858–872.

Tran, T.H., Polyakov, G.V., Tran, T.A., Borisenko, A.S., Izokh, A.E., Balykin, P.A., Ngo, T.P., and Pham, T.D., 2016, Intraplate magmatism and metallogeny of North Vietnam: Switzerland, Springer International Publishing, 372 p.

Tran, V.T., 2000, Mineral resources map of Vietnam: Hanoi, Department of Geology and Minerals of Vietnam, no. 142/QD-CXB, scale 1:1,000,000.

Turner, S., Arnaud, H., Liu, J., Rogers, N., Hawkesworth, C.J., Harris, N., Kelley, S., van Calsteren, P., and Deng, W.M., 1996, Post-collision, shoshonitic volcanism on the Tibetan Plateau: Implications for convective thinning of the lithosphere and the source of ocean island basalts: Journal of Petrology, v. 37, p. 45–71.

Usuki, T., Lan, C.Y., Tran, T.H., Phan, T.D., Wang, K.L., Shellnutt, G.J., and Chung, S.L., 2015, Zircon U-Pb ages and Hf isotopic compositions of alkaline silicic magmatic rocks in the Phan Si Pan-Tu Le region, northern Vietnam: Identification of a displaced western extension of the Emeishan large igneous province: Journal of Asian Earth Sciences, v. 97, p. 102–124.

Valley, J.W., Lackey, J.S., Cavosie, A.J., Clechenko, C.C., Spicuzza, M.J., Basei, M.A.S., Bindeman, I.N., Ferreira, V.P., Sial, A.N., and King, E.M., 2005, 4.4 billion years of crustal maturation: Oxygen isotope ratios of magmatic zircon: Contributions to Mineralogy and Petrology, v. 150, no. 6, p. 561–580.

van Hinsbergen, D.J., Steinberger, B., Doubrovine, P.V., and Gassmöller, R., 2011, Acceleration and deceleration of India-Asia convergence since the Cretaceous: Roles of mantle plumes and continental collision: Journal of Geophysical Research: Solid Earth, v. 116, article B06101.

Wang, C., Liu, J., Zhang, H., Zhang, X., Zhang, D., Xi, Z., and Wang, Z., 2020, Geochronology and mineralogy of the Weishan carbonatite in Shandong province, eastern China: Geoscience Frontiers, v. 10, no. 2, p. 769–785.

Wang, J., Su, B.X., Chen, C., Ferrero, S., Malaviarachchi, S.P.K., Sakyi, P.A., Yang, Y.H., and Dharmapriya, P.L., 2021, Crustal derivation of the ca. 475 Ma Eppawala carbonatites in Sri Lanka: Journal of Petrology, v. 62, no. 11, article egab075.

Wang, W., Cawood, P.A., Zhou, M.F., and Zhao, J.H., 2016, Paleoproterozoic magmatic and metamorphic events link Yangtze to northwest Laurentia in the Nuna supercontinent: Earth and Planetary Science Letters, v. 433, p. 269–279.

Wang, X., Metcalfe, I., Jian, P., He, L., and Wang, C., 2000, The Jinshajiang-Ailaoshan suture zone, China: Tectonostratigraphy, age and evolution: Journal of Asian Earth Sciences, v. 18, p. 675–690.

Wang, X.S., Williams-Jones, A.E., Bi, X.W., Hu, R.Z., Xiao, J.F., and Huang, M.L., 2019, Late Cretaceous transtension in the eastern Tibetan Plateau: Evidence from postcollisional A-type granite and syenite in the Changdu area, China: Journal of Geophysical Research: Solid Earth, v. 124, p. 6409–6427.

Wang, Y., Qian, X., Cawood, P.A., Liu, H., Feng, Q., Zhao, G., Zhang, Y., He, H., and Zhang P., 2018, Closure of the East Paleotethyan Ocean and amalgamation of the Eastern Cimmerian and Southeast Asia continental fragments: Earth-Science Review, v. 186, p. 195–230.

Wang, Y., Fan, W., Zhang, Y., Peng, T., Chen, X., and Xu, Y., 2006, Kinematics and $^{40}Ar/^{39}Ar$ geochronology of the Gaoligong and Chongshan shear systems, western Yunnan, China: Implications for early Oligocene tectonic extrusion of SE Asia: Tectonophysics, v. 418, no. 3, p. 235–254.

White, L.T., and Lister, G.S., 2012, The collision of India with Asia: Journal of Geodynamics, v. 56–57, p. 7–17.

Woodard, J., and Hetherington, C.J., 2014, Carbonatite in a postcollisional tectonic setting: Geochronology and emplacement conditions at Naantali, SW Finland: Precambrian Research, v. 240, p. 94–107.

Woolley, A.R., and Bailey, D.K., 2012, The crucial role of lithospheric structure in the generation and release of carbonatites: Geological evidence: Mineralogical Magazine, v. 76, p. 259–270.

Woolley, A.R., and Kjarsgaard, A., 2008, Carbonatite occurrences of the world: Map and database: Geological Survey of Canada, Open File 5796.

Wu, H., Zhu, W., and Ge, R., 2022, Evidence for carbonatite derived from the earth's crust: The late Paleoproterozoic carbonate-rich magmatic rocks in the southeast Tarim craton, northwest China: Precambrian Research, v. 369, article 106425.

Xie, Y., Li, Y., Hou, Z., Cooke D.R., Danyushevsky, L., Dominy, S.C., and Yin, S., 2015, A model for carbonatite hosted REE mineralisation—the Mianning-Dechang REE belt, Western Sichuan Province, China: Ore Geology Reviews, v. 70, p. 595–612.

Xu, C., Chakhmouradian, A.R., Taylor, R.N., Kynicky, J., Li, W.B., Song, W.L., and Fletcher, I.R., 2014, Origin of carbonatites in the south Qinling orogen: Implications for crustal recycling and timing of collision between the South and North China blocks: Geochimica et Cosmochimica Acta, v. 143, p. 189–206.

Yang, K.F., Fan, H.R., Pirajno, F., and Li, X.C., 2019, The Bayan Obo (China) giant REE accumulation conundrum elucidated by intense magmatic differentiation of carbonatite: Geology, v. 47, p. 1198–1202.

Yang, L., Wang, Q., Groves, D.I., Lu, S., Li, H., Wang, P., and Deng, J., 2021, Multiple orogenic gold mineralization events in a collisional orogen: Insights from an extruded terrane along the southeastern margin of the Tibetan Plateau: Journal of Structural Geology, v. 147, article 104333.

Yang, Y.H., Wu, F.Y., Li, Q.L, Rojas-Agramonte, Y., Yang, J.H., Li, Y., Ma, Q., Xie, L.W., Huang, C., Fan, H.R., Zhao, Z.F., and Xu, C., 2019, In situ U-Th-Pb dating and Sr-Nd isotope analysis of bastnasite by LA-(MC)-ICP-MS: Geostandards and Geoanalytical Research, v. 43, p. 543–565.

Yang, Y.Z., Long, Q., Hu, H.T., Hieu, P.T., Nguyen, T.B.T., and Chen, F.K., 2013, Geochemical characteristics and origin of lamprophyre in the Laichau area, northwestern Vietnam: Acta Petrologica Sinica, v. 29, p. 899–911.

Yin, A., and Harrison, T.M., 2000, Geologic evolution of the Himalayan-Tibetan orogen: Annual Review of Earth and Planetary Sciences, v. 28, p. 211–280.

Yin, A., Rumelhart, P.E., Butler, R., Cowgill, E., Harrison, T.M., Foster, D.A., Ingersoll, R.V., Zhang, Q., Zhou, X., Wang, X.F., et al., 2002, Tectonic history of the Altyn Tagh fault system in northern Tibet inferred from Cenozoic sedimentation: Geological Society of America Bulletin, v. 114, no. 10, p. 1257–1295.

Zaitsev, A.N., Williams, C.T., Jeffries, T.E., Strekopytov, S., Moutte, J., Ivashchenkova, O.V., Spratt, J., Petrov, S.V., Wall, F., Seltmann, R., and Borozdin, A.P., 2014, Rare earth elements in phoscorites and carbonatites of the Devonian Kola alkaline province, Russia: Examples from Kovdor, Khibina, Vuoriyarvi and Turiy Mys complexes: Ore Geology Reviews, v. 61, p. 204–225.

Zhang, W., Chen, W.T., Gao, J.F., Chen, H.K., and Li, J.H., 2019, Two episodes of REE mineralization in the Qinling orogenic belt, Central China: In-situ U-Th-Pb dating of bastnäsite and monazite: Mineralium Deposita, v. 54, p. 1265–1280.

Zhu, D.C., Wang, Q., Zhao, Z.D., Chung, S.L., Cawood, P.A., Niu, Y., Liu, S.A., Wu, F.Y., and Mo, X.X., 2015, Magmatic record of India-Asia collision: Scientific Reports, v. 5, article 14289.

Zhu, D.C., Li, S.M., Cawood, P.A., Wang, Q., Zhao, Z.D., Liu, S.A., and Wang, L.Q., 2016, Assembly of the Lhasa and Qiangtang terranes in central Tibet by divergent double subduction: Lithos, v. 245, p. 7–17.

Xiaochun Li is an associate professor at the Institute of Geology and Geophysics, Chinese Academy of Sciences. He received his B.Sc. degree from Nanjing University, China, in 2009, and his Ph.D. degree from The University of Hong Kong in 2016. His research interests include studies of REE deposits, iron oxide copper-gold deposits, and accessory minerals. His recent research is focused on carbonatite-related REE deposits, such as Bayan Obo and Weishan in China and Dong Pao and Nam Xe in Vietnam.